

Supplementary Materials for **Stellate cells drive maturation of the entorhinal-hippocampal circuit**

Flavio Donato,* R. Irene Jacobsen, May-Britt Moser, Edvard I. Moser*

*Corresponding author. Email: flavio.donato@ntnu.no (F.D.); edvard.moser@ntnu.no (E.I.M.)

Published 2 February 2017 on *Science* First Release
DOI: 10.1126/science.aai8178

This PDF file includes:

Materials and Methods
Figs. S1 to S14
References

Supplementary methods:

Virus injection in the adult.

On the day of surgery, adult mice (P60-P365) were anesthetized and analgesics were provided (Rymadil, Pfizer, intraperitoneal injection, 5 mg/kg; Temgesic, Schering-Plough, local subcutaneous injection, 0.05 mg/kg; Marcain, AstraZeneca, subcutaneous injection, 1 mg/kg). A high titer of rAAV was injected into the target areas using a 5 μ l Neuro Syringe (Hamilton Company, USA) with a 33-gauge metal needle. The virus carried a Cre-dependent construct for expression of the marker protein mCherry (AAV1-CAG-FLEX-mCherry, UPenn Vector Core, University of Pennsylvania). Injection volume (up to 200 nl at each location for a maximum amount of 500 nl) and flow rate (0.1 μ l/min) were controlled with a Micro4 Microsyringe Pump Controller (World Precision Instruments). Two injection sites were used to target the MEC at a medial and a lateral location (48). The medial injection was performed at 3.4 mm lateral to bregma, 0.3 mm anterior to the transverse sinus, at 3 locations in depth (1.7, 1.5 and 1.3 mm from the dura surface). The lateral injection was performed at 4 mm lateral to bregma, 0.2 mm anterior to the transverse sinus, at 2 location in depth (1.5 and 1.3 mm from the dura surface). After the injection, the needle was kept in position for 10 minutes before retraction. Finally, the skin was sutured, and the animal allowed to recover in a heated chamber (38°C, 30-90 minutes) until it regained complete mobility and alertness.

Temporal specificity of in utero viral labelling.

To verify the temporal specificity of the viral labelling, we used a combined viral/BrdU approach. Ultrasound imaging was used to target the viral solution (AAV1-CaMKII-Cre) into the developing lateral ventricle at E13 as described in the main methods section. BrdU (5-Bromo-2'-deoxyuridine \geq 99% (HPLC), Sigma-Aldrich, 100 mg/Kg) was injected intraperitoneally in the pregnant mother at different intervals from the embryonic AAV injections, which was defined as time 0 in our time course. A second injection, aimed at the MEC, was performed in adult animals (P60-P90) as described above, and carried a Cre-dependent construct to highlight the cells targeted in utero. For every time point of BrdU

injection, we quantified the fraction of cells labelled by the virus that also exhibited BrdU reactivity in the nucleus.

Histology, staining and confocal imaging.

Mice received an overdose of sodium pentobarbital before transcardial perfusion with freshly prepared PFA (4% in PBS, flow of 2 ml/min). Samples were sliced on a cryostat (30-50 µm thick sections) and stained for immunodetection of specific proteins. Briefly, floating sections were incubated overnight with the primary antibody diluted in a solution of PBS + 0.3% Triton + 3% BSA; washed 3 times with PBS + 0.3% Triton; incubated for 1h at room temperature with the secondary antibody diluted in a solution of PBS + 0.3% Triton + 3% BSA; washed with PBS 3 times and then mounted on a slide (ProLong Gold Antifade used as embedding medium, Invitrogen). Primary antibodies were as follows: Rabbit anti NeuN (1:1000, AbCam), Mouse anti NeuN (1:200, Millipore), Mouse anti Reelin (1:200, MBL International), Rabbit anti Calbindin (1:1000, Swant), Goat anti Parvalbumin (1:10000, Swant), Goat anti Doublecortin (1:200, Santa Cruz Biotechnology), Rabbit anti c-FOS (1:1000, Santa Cruz Biotechnology) Mouse anti Bassoon (1:200, RY), Rat anti BrdU (1:500, Abcam). Different antibody combinations were applied to the same sections during individual reactions, according to the proteins under study. Secondary antibodies were reactive to the species that hosted the production of the primary antibodies, and conjugated to Alexa fluorophore 488, 568 or 647 (1:500, Molecular Probes).

BrdU labeling *in vivo* was carried out at 24h intervals as previously described (54). Briefly, we injected mice with BrdU (5-Bromo-2'-deoxyuridine ≥99% (HPLC), Sigma-Aldrich; 100 mg/kg) at defined times during embryonic development, and analyzed brain sections of 3 month old mice for BrdU labeling. Only strongly BrdU-labeled cells that did not undergo further rounds of DNA replication and cell division subsequent to BrdU incorporation were included in the analysis.

For confocal imaging, an LSM 510 Meta and a Zeiss LSM 880 microscope (Carl Zeiss, Germany) were used. Samples belonging to the same experiment (samples from experimental mice at a given time point, with their controls) were acquired in parallel and with the same

settings (laser power: 2–15%; optical slice: 1.28–1.35 airy units, step size: 2 μm for population analysis; 0.5 μm for synaptic analysis) using an EC Plan-Neofluar 20 \times /0.8 air immersion, 40 \times /1.3 oil immersion, and 63 \times /1.4 oil immersion objective (Zeiss). Before acquisition, gain and digital offset were established on sections from control animals to optimize the dynamic range of acquisition to the dynamic range of the staining (baselines were set independently for every staining based on the protein under investigation, see the following paragraphs). Pixel size was optimized for synaptic detection (200 nm axial resolution). Settings were kept constant during acquisition.

Automatic identification of BrdU, NeuN, Doublecortin, Reelin, Calbindin, Parvalbumin or c-FOS expressing cells was performed with commercially available software (ImageJ; Imaris, Bitplane). For the analysis of Doublecortin (DCX) expression, cells were first identified by the expression of the neuronal marker NeuN (NeuN+), Reelin (Rl+) or Calbindin (Cb+). Then the average intensity values of pixels in the somas of identified cells were compared to a baseline threshold to determine the level of DCX fluorescence. The threshold was set to the average level of fluorescence of pixels located in the nucleus of excitatory cells (DCX is excluded from the nuclear compartment, which hence constitutes an ideal baseline for evaluating expression, (20)). Neurons were considered as Doublecortin negative (DCX-) when the intensity of fluorescence of DCX in the soma fell below the threshold value. We limited analysis to the internal portion of the soma by excluding the subcortical portion of the cell (about 3 μm below the cell membrane) from further analysis, to avoid bleed-through of extracellular signal into the cell under study. DCX downregulation was expressed as the fraction of NeuN+ neurons with undetectable levels of DCX at the specific anatomical location under investigation (see below), giving a range from 0 (all NeuN+ cells are DCX+) to 1 (all NeuN+ are DCX-).

For the analysis of maturation in the fast-spiking interneuron network, parvalbumin (PV) expressing somas were detected using an immunological marker. Cells were considered positive when the expression of PV exceeded the noise level set at the intensity value of the extracellular matrix. The number of PV+ cells was subsequently normalized to the number of positive neurons detected in adult animals (P90-P120) in a comparable volume of tissue. We did not distinguish between high and low-expressing PV interneurons, because the difference

between these two subtypes of interneurons, linked to different regulations of plasticity in adult cortical circuits, is not expressed until approximately P60 in the mouse (55).

For the analysis of c-FOS expression, cells were first identified by expression of the neuronal marker NeuN (NeuN+). Then the average intensity values of pixels in the soma of identified cells were compared to a baseline threshold to determine the level of c-FOS fluorescence. The threshold was set to the average level of fluorescence of pixels located in the extracellular matrix (defined as the portion of the neuropil devoid of NeuN signal). We then quantified the fraction of the NeuN+ neurons with c-FOS expression at the specific anatomical location under investigation (see below), giving a range from 0 (all NeuN+ cells are c-FOS-) to 1 (all NeuN+ are c-FOS+).

For the analysis of synaptogenesis, Bassoon expressing puncta (Bs+) were automatically identified with commercially available software (ImageJ; Imaris, Bitplane). Baseline was set at pixel intensity values found in the nucleus. The number of Bs puncta was then normalized to the number of puncta detected in adult animals (P60-P120) in a comparable volume of neuropil (neuropil volume was calculated by subtracting the volume occupied by cell somas and neuronal processes, identified by NeuN+ signal, from the total volume under investigation). We analyzed nine independent field of views from each region in the network. The nine areas were chosen to minimize the volume occupied by blood vessels, which were excluded from the analysis.

For analysis of neurogenesis, BrdU injections were performed on each consecutive day between E10 and E17 (the dam of each litter was injected once). Injections at E10 and E17 did not label any cells in the adult, thereby marking the beginning and end of MEC-L2 neurogenesis. Reelin+ (RI), calbindin+ (Cb) and parvalbumin+ (PV) cells were considered BrdU+ if the nucleus exhibited non-zero levels of fluorescence for BrdU (baseline set at the pixel intensity value found in the soma). BrdU labelling was expressed as the fraction of the RI/Cb/PV expressing neurons with nuclear labelling for BrdU.

Due to the topographic organization of the entorhinal-hippocampal network, we focused our analysis on the dorsal portion of the entorhinal cortex and hippocampus (EC: up to 500 μ m from the border to postrhinal cortex, 3.5mm lateral to the midline). Local network analysis in the MEC network was conducted at discrete positions long the dorsoventral axis by subdividing the longitudinal extent of the MEC into eight blocks of equal dimension (each 375 μ m in length). The dorsal and ventral borders of the MEC were identified by using as references the sharp transition in layer 2 cell density at each end (position 0 in Fig 3A corresponding to MEC to postrhinal cortex transition; position 3000 corresponding to MEC to LEC transition at the medio-lateral level of the CNS where the analysis was conducted, 3.2-3.6 mm lateral to the midline).

Statistical analysis.

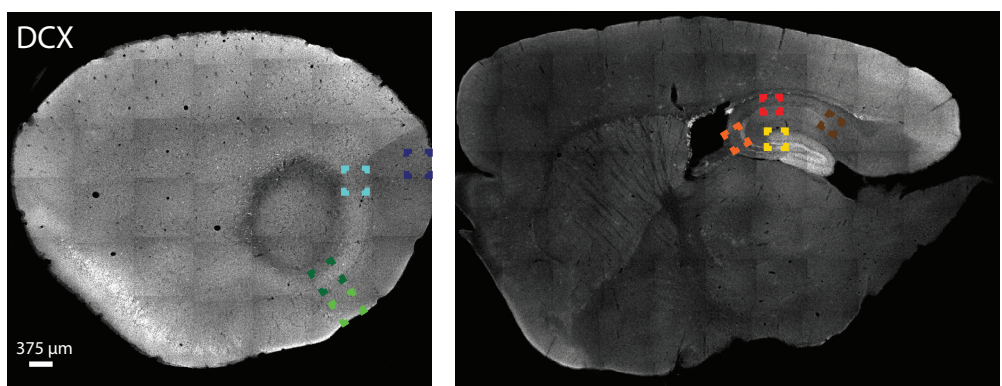
Statistical analysis was conducted with commercially available software; Prism 6.0 (Graphpad) and Matlab (Mathworks). P values considered significant were <0.05 . All comparisons performed were between sets of independent measures (measurements were performed on different sets of animals, without any repeated measure from an individual subject).

To assess statistical significance of developmental time courses and neurogenesis time courses, we used a 2-way ANOVA. Group and Segment were defined as factors for comparisons of local networks along the dorso-ventral MEC. In the developmental time course experiments, we first performed a global analysis between datasets collected at every time point for each of the three variables under investigation (fraction of DCX– stellate cells, fraction of DCX– pyramidal cells and fraction of adult interneurons expressing PV). In the silencing experiments, we subsequently performed pairwise comparisons for each of the three variables under investigation. Independent analysis was also conducted between each silenced group and its controls. In the neurogenesis analyses, we first performed a global analysis between datasets collected at every segment along the dorso-ventral axis of the MEC for each of the three variables under investigation (individual analysis for the fraction of DCX– stellate cells, fraction of DCX– pyramidal cells and fraction of the adult interneurons expressing PV); then a pairwise analysis was conducted for every possible combination among time points across individual segments. To assess statistical significance between control and silenced animals, we used the Student’s t-test and the Mann-Whitney-Wilcoxon test.

To investigate similarities in the maturation time courses across nodes of the entorhinal-hippocampal network, we conducted an unbiased clustering analysis. Hierarchical clustering was performed to obtain two types of information: the equivalence between nodes of the dendograms to define structures with comparable time courses of maturation, and the hierarchy of nodes to establish the temporal sequence of the process under investigation. For the hierarchical clustering in Fig. 1D, we used the Machine Learning Toolbox and Statistic Toolbox in Matlab (Mathworks). The length of the links (horizontal bars) in the dendograms represents the similarity between the connected nodes. The null hypothesis of the analysis is that all the structures exhibit comparable maturation profiles.

Fig. S1

A



B

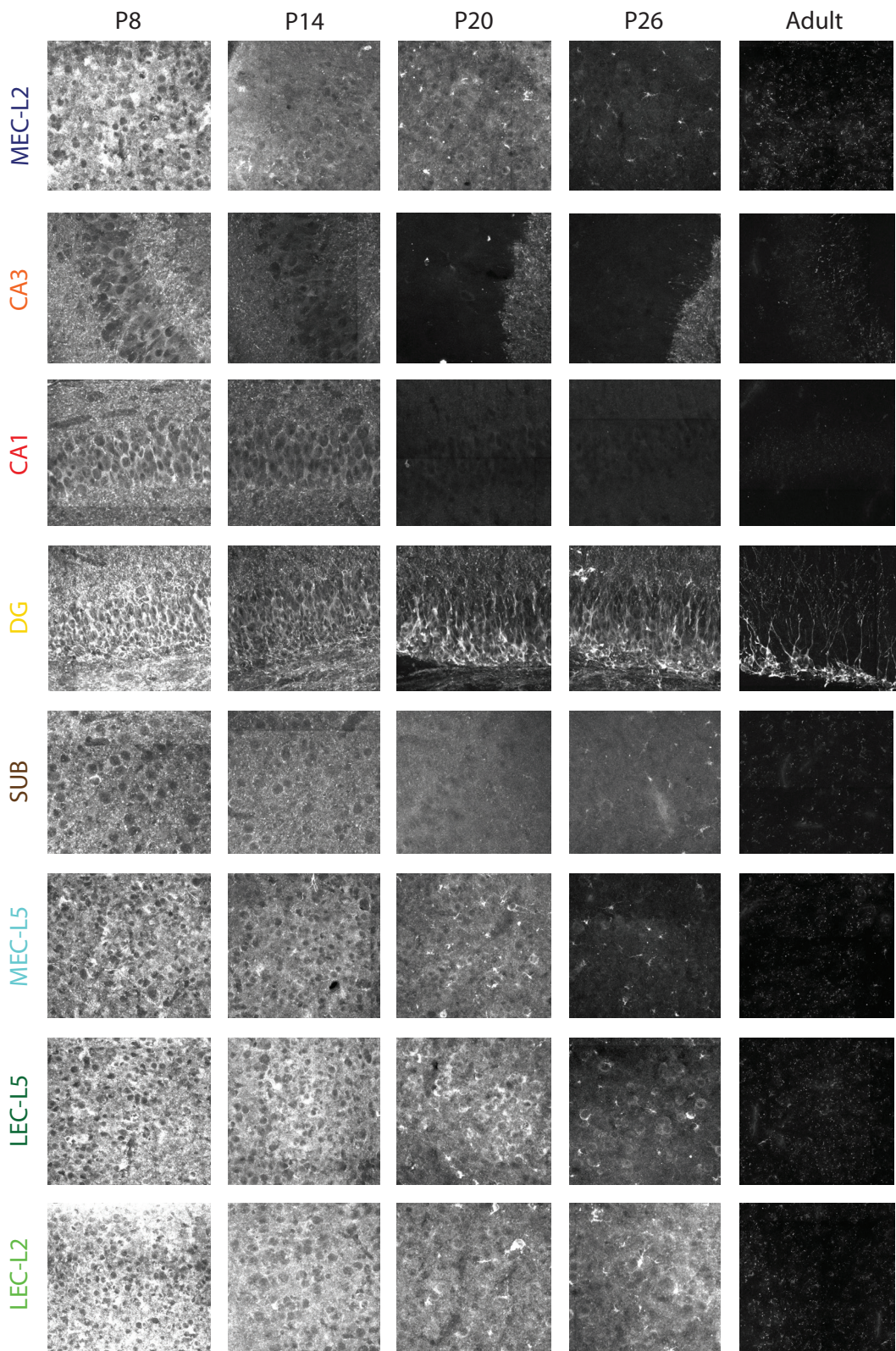
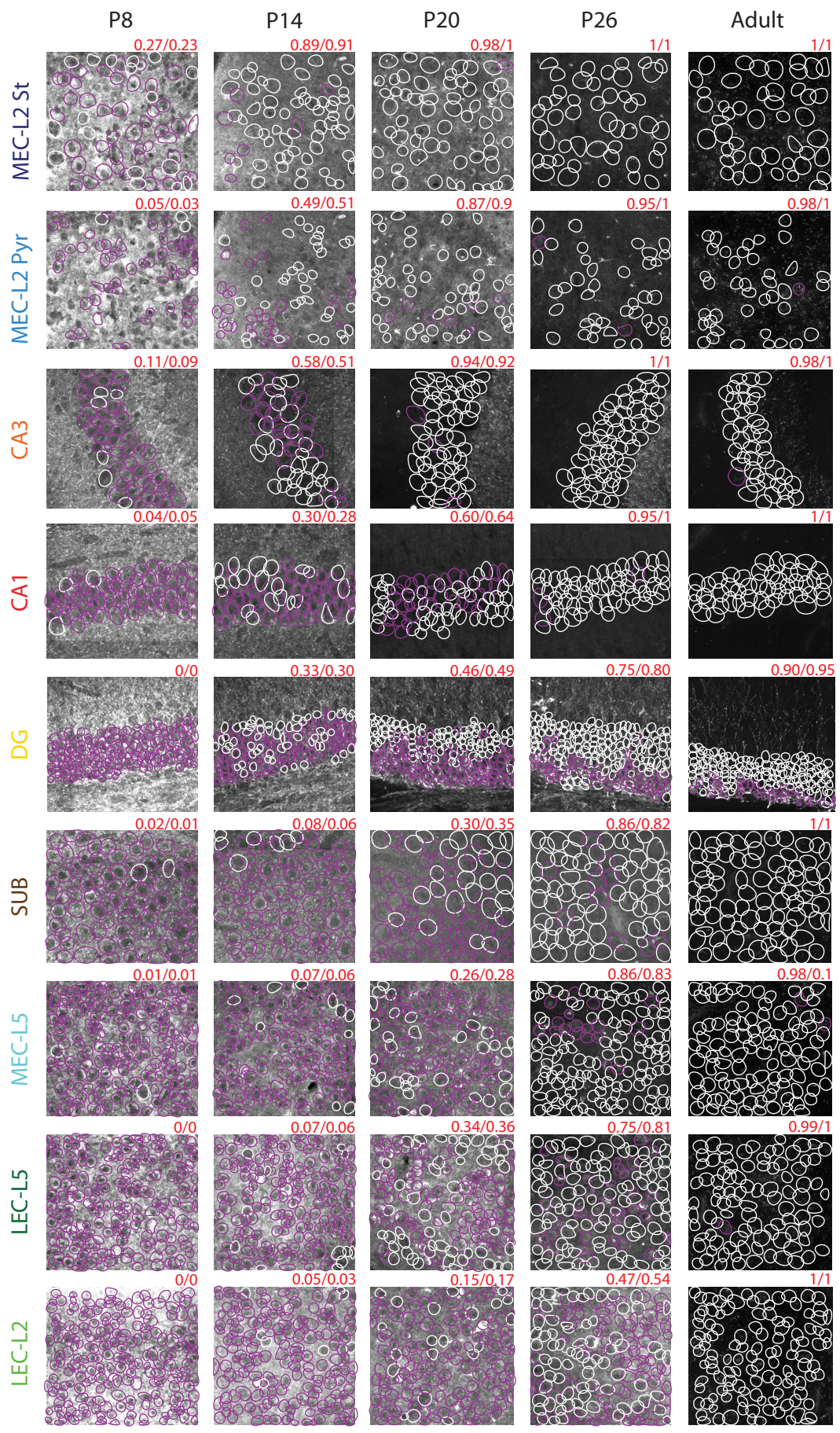
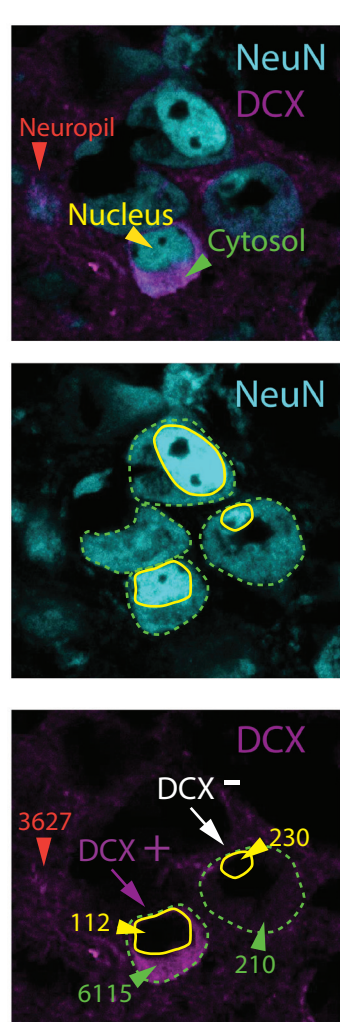


Fig. S1(Continued)

C



D

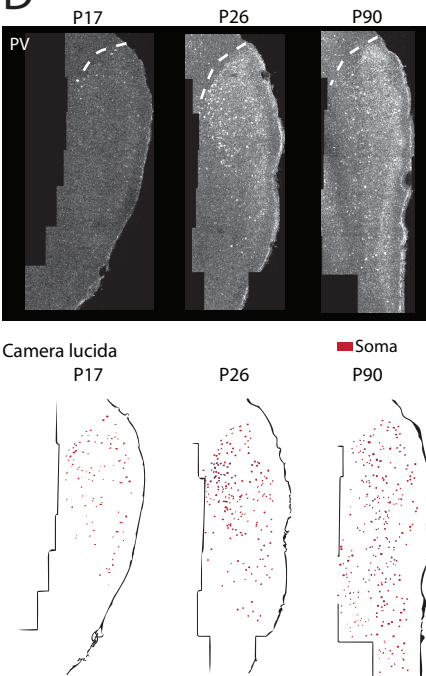


Fig. S1 Change in doublecortin expression across the entorhinal-hippocampal network during postnatal development.

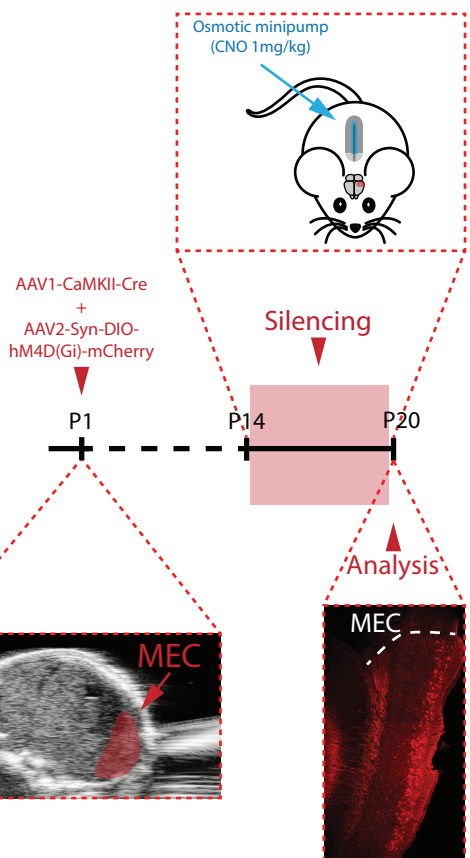
(A) 10 \times confocal images with color-coded boxes showing the location of high-magnification images in (B). Sections are sagittal and show two different medio-lateral levels (through dorsal entorhinal cortex and hippocampus, respectively). Doublecortin (DCX) in white. (B) Confocal images showing DCX (white) across subregions of the entorhinal-hippocampal circuit at multiple time points during the first postnatal month (image locations as indicated in A). Validation of the quantification came from comparisons with adult expression levels (right panels; note exclusive expression in the dentate gyrus). Single fields of view were acquired with a 40 \times /1.3NA oil immersion objective (zoom 0.6 \times), and processed together, using constant parameters. Maximum intensity projections from 3D stacks recapitulate the quantification of DCX- cells presented in Fig. 1C. In CA3 panels, note high level of DCX immunoreactivity to the right, which reflects mossy fiber inputs from immature granule cells. (C) Left panels: 40 \times single confocal plane image of a cluster of 4 principal cells in MEC-L2 (NeuN+, cyan; Doublecortin, DCX, Magenta). Cytosolic signal (green arrows) and nuclear signal (yellow arrows) were distinguished from neuropil signal (orange arrows) by the expression of the neuronal marker NeuN (NeuN+) and either Reelin (Rl+) or Calbindin (Cb+) (NeuN staining is shown in the upper and middle panels). The average intensity values of pixels representing Doublecortin signal (DCX) were compared across identified cellular compartments (bottom panel, arbitrary units). In single cells, if the cytosolic signal exceeded the nuclear signal, the cell was considered to be DCX+ (cell identified by magenta arrow in lower panel; DCX is not present in the nuclear compartment, which hence constitutes an ideal baseline for evaluating expression (20)). Neurons were considered DCX negative (DCX-) when the intensity of fluorescence of DCX in the cytosol fell below the value for the nucleus (cell identified by white arrow in the lower panel). Neuropil signals were often as bright as cytosolic signals (Fig. S1B), and hence might contribute substantially to the fluorescence in cortical areas, but in the present analysis the neuropil signal was excluded from consideration. Right panels: processed dataset from (B). Individual neurons (identified automatically based on the expression of somatic markers, as in the left panels) have been labelled as regions of interest (ROI), and each individual ROI has been hand-drawn onto the maximum intensity projection of the DCX signal across the 3D dataset. Single ROIs (solid circles) are colour coded based on presence (magenta) or absence (white) of DCX, following the procedure in the left panels. Note that the overall

level of fluorescence present in specific regions of an image (hippocampus), or diffused through the whole extent of the cell layer (cortex), can be the result of neuropil contamination, which has been excluded from our single-cell analysis as previously explained. Above each image, its proportion of DCX- cells , compared to the mean value across animals (left and right side of slash, respectively; means as in Fig. 1C) is indicated. **(D)** Automatic quantification and analysis of parvalbumin-expressing neurons (PV+). Automatically detected somas of PV+ neurons (for detailed procedure, see Methods) were mapped along the dorso-ventral extent of the MEC to achieve local density estimates. Upper panels: 40 \times confocal images of sagittal sections from 3 different time points during postnatal development. Immunodetection was used to reveal PV expression (white) in the soma and neuropil processes of interneurons. Images are maximum intensity projections. Lower panels: camera lucida of upper panels. Each red dot is a PV+ soma.

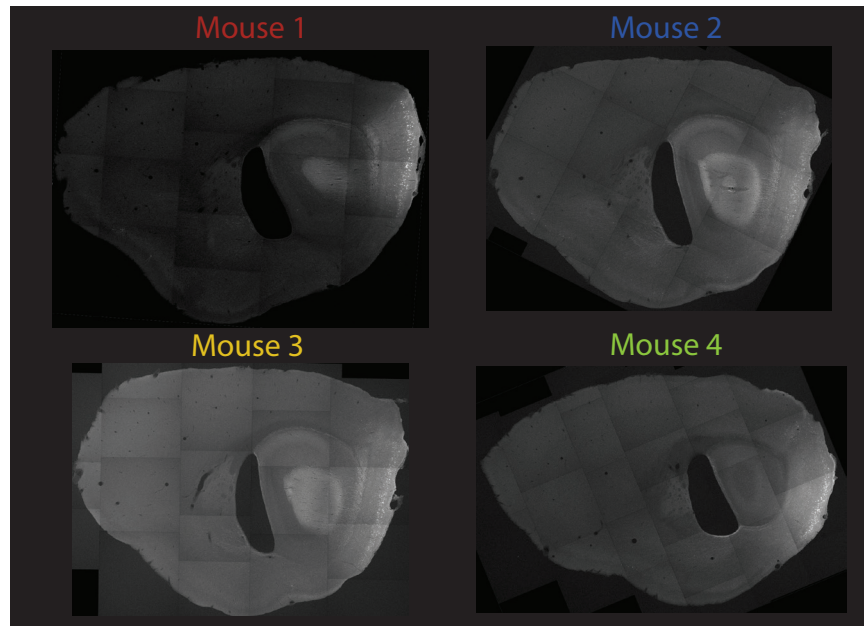
Fig. S2

A

Experiment timeline:



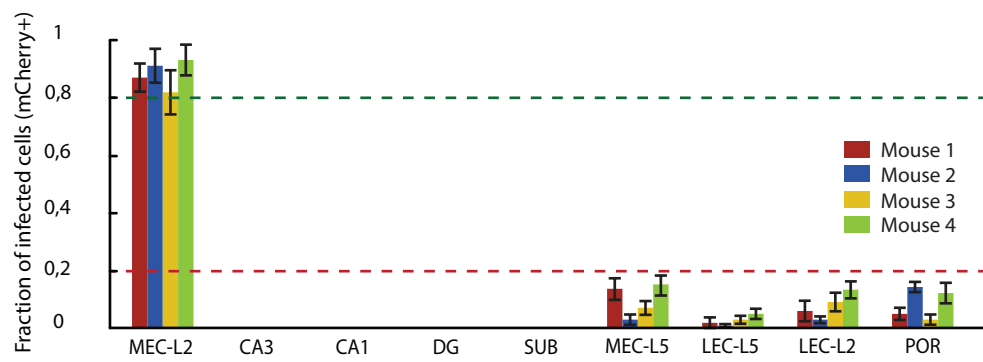
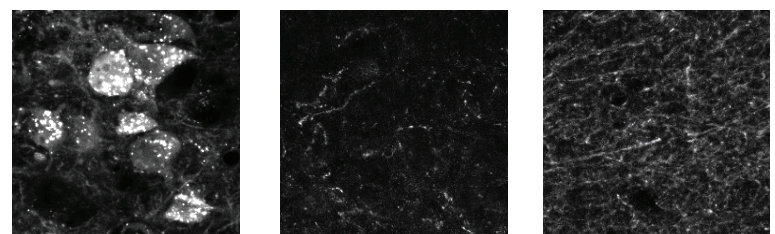
B



MEC-L2

MEC-L5

CA1



C

	MEC-L2	Hippocampus	LEC
MEC-L2	+	-	-
MEC-L5	-	-	-
LEC-L5	-	-	+
LEC-L2	-	-	+
DG	-	-	-
CA3	-	+	-
CA1	-	+	-
SUB	-	-	-
POR	-	-	-

D

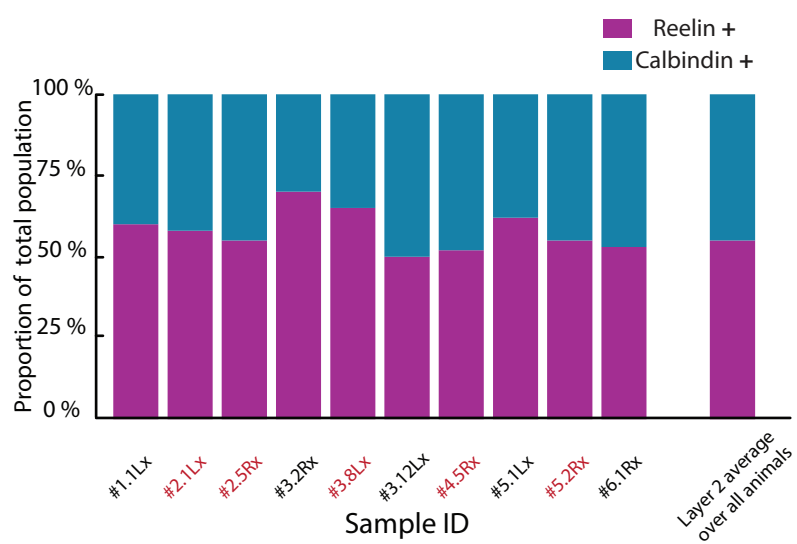


Fig. S2: Specificity of hM4D(Gi) expression after viral infection on postnatal day 1.

(A) Schematic illustration of experiment involving pharmacogenetic silencing of excitatory neurons in the entorhinal-hippocampal network during postnatal development. A viral mix (AAV1-CaMKII-Cre and AAV2-Syn-DIO-hM4D(Gi)-mCherry, 1:1) was injected into the brain of newborn pups at P1 in order to express hM4D(Gi) selectively in excitatory neurons, under the control of a CaMKII promoter. Injections were directed to MEC-L2, hippocampus or LEC, using ultrasound to identify structural landmarks and guide the pipette (bottom left). The anatomical specificity of the infection was later verified by imaging serial sections of the injected hemisphere, using mCherry expression as an indicator of infected cells (bottom right; 20 \times confocal image of a sagittal section from a P20 animal, maximum intensity projection). Somas of infected neurons were located selectively in the target area (MEC-L2). Staining in deep layers and hippocampus reflect axons only. Top panel: Pharmacogenetic silencing of virally infected neurons was performed two weeks after injection through continuous delivery of the ligand CNO (1 mg/kg) by an osmotic minipump implanted subcutaneously on the pups' backs. CNO was delivered at a constant rate over the course of several days during maturation, typically from P14 to P20. Quantitative analysis of maturational markers was conducted on P20, at the end of the silencing window. In a subset of animals, CNO was delivered from P11 to P14. **(B)** Spread of viral infection in P1-injected animals. Upper panel: 10 \times confocal images of sagittal sections from 4 injected animals with selective infection in MEC-L2. White: mCherry signal. Images are maximum intensity projections (MIPs). Middle panels: 40x MIPs of infected cells in MEC-L2, MEC-L5 and axonal tracts in hippocampal area CA1 (pictures from Mouse 1). Lower panel: Fraction of NeuN+ neurons in every area with mCherry expression (mean \pm S.D., same 4 animals as in the upper panel). An area was considered infected when more than 80% of the NeuN+ neurons (green dashed line) expressed mCherry (virus-positive, + in panel C), and non-infected when mCherry was expressed in fewer than 20% of NeuN+ neurons (red dashed line; virus-negative, - in C). mCherry expression was taken as an indication of effective expression of the hM4D(Gi) construct. Mice with infection rates between the two cut-offs were excluded from further analysis (unless otherwise stated, Fig. S6). 102 out of 192 injected hemispheres were included in the analysis. **(C)** Overview quantification of anatomical spread of the viral infection. Based on areas exhibiting viral expression, animals were subdivided into multiple categories for analysis (MEC-L2 specific; hippocampus specific; LEC specific; + and - as described in (B)). **(D)** In MEC-L2, the viral mix did not exhibit any tropism for either stellate or pyramidal cells. We verified the identity of mCherry+ cells with

molecular markers selective for either stellate or pyramidal cells (reelin or calbindin, respectively). Local network analysis in individual animals confirmed that the proportion of stellate/pyramidal cells among the infected neurons for each animal was comparable to the average found in the MEC-L2 network across multiple animals (> 400000 neurons from over 50 animals analyzed). *x* axis: identification codes of samples analyzed in Fig 2A and 3C. Each cumulative bar represents one animal. Silenced animals: red labels. Control animals (No Virus, CNO): black labels. *y* axis: proportions indicating relative abundance of reelin+ neurons (magenta) and calbindin+ neurons (cyan) within each population of mCherry+ neurons.

Fig. S3

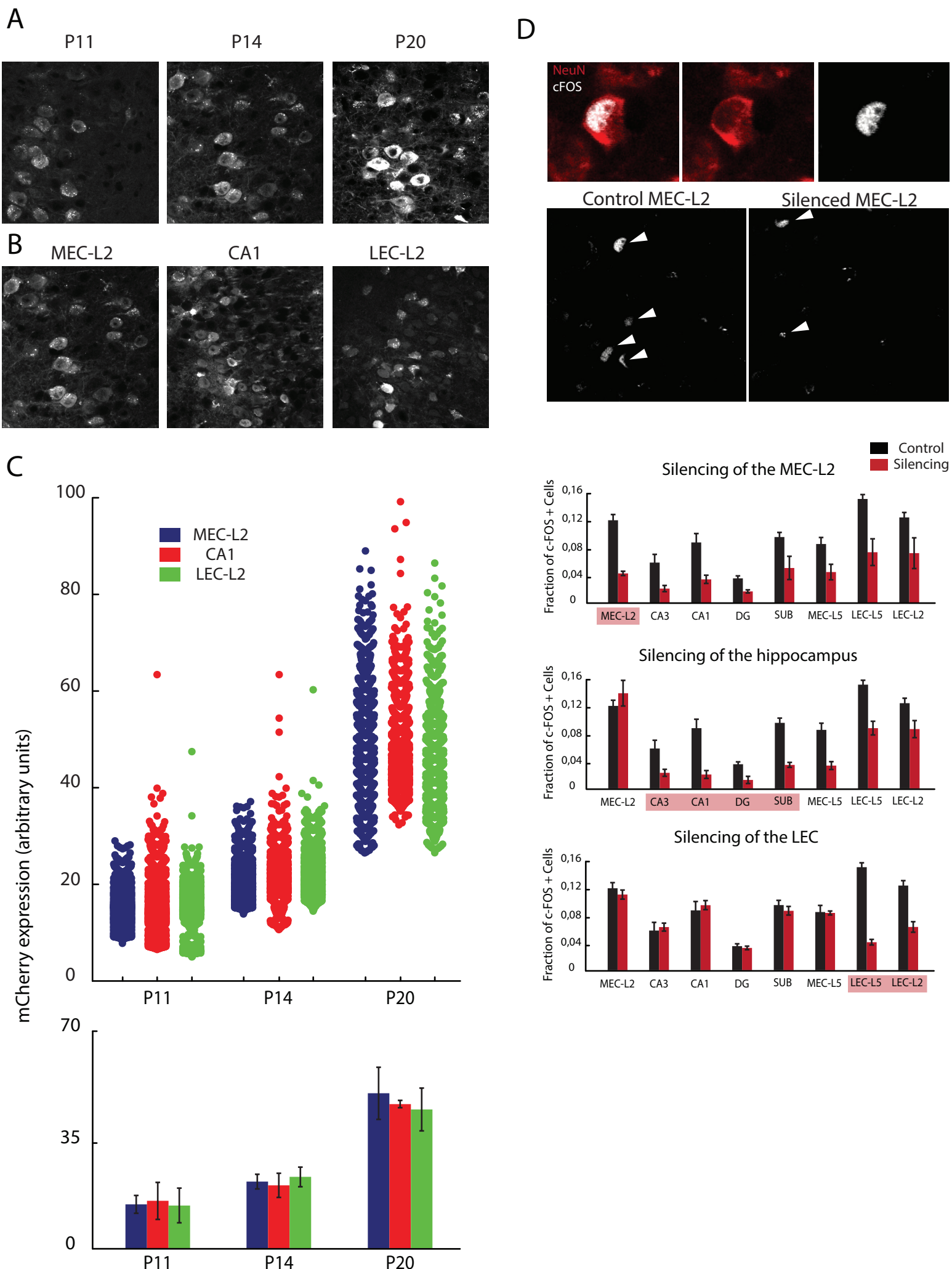
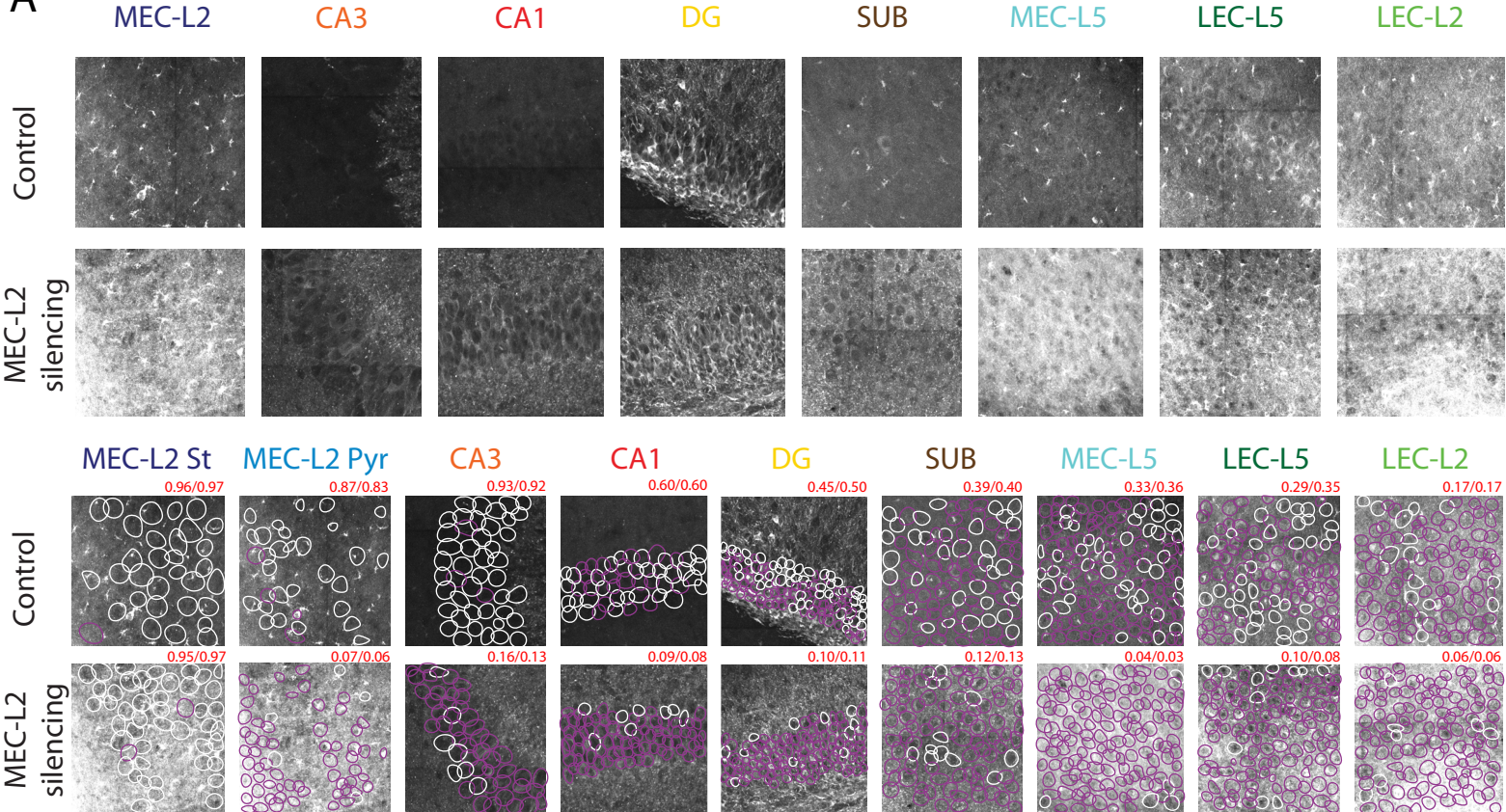


Fig S3: Time course of hM4D(Gi) expression in infected neurons and validation of silencing.

(A) 40 \times single confocal planes showing mCherry expression (white) in MEC-L2 excitatory neurons at three postnatal ages (P11, P14 and P20). **(B)** 40 \times single confocal planes showing mCherry expression (white) in excitatory neurons of MEC-L2, CA1, and MEC-L2 at P14. **(C)** Quantification of mCherry expression in infected neurons of MEC-L2 (blue), CA1 (red) and LEC-L2 (green) across multiple ages. Single isosurfaces were built in Imaris around somas identified by mCherry fluorescence, and the mean intensity of the pixels included in the isosurfaces (expressed in arbitrary units, y axis) was taken as an indication of the level of mCherry expression in a single cell. Upper panel: values from single cells were pooled across animals for each experimental condition (each dot represents one neuron). Lower panel: bars represent average values across animals (means \pm S.D.; >16000 neurons from 15 animals). **(D)** Upper panels: high magnification (60 \times) single confocal planes showing c-FOS expression (white) in neurons of MEC-L2 (NeuN, red) from a control mouse. Middle panels: low magnification (28 \times) single confocal planes showing c-FOS expression (white) in MEC-L2 of control (left) and silenced (right) animals. Lower panels: fraction of NeuN+ neurons with nuclear expression of c-FOS (c-FOS+) across subdivisions of the entorhinal-hippocampal circuit in control animals (black) and silenced animals (red). y axis: Fraction of double positive NeuN/c-FOS neurons. DREADD-mediated silencing induces a decrease in c-FOS expression in areas expressing the viral construct (x axis, red boxes) as well as downstream stations of the transverse hippocampal circuit (mean \pm S.D., Student's t-test comparisons to controls, $t > 6.5$ and $P < 0.035$, $t < 1.63$ and $P > 0.52$ for comparisons with areas upstream of the infection site).

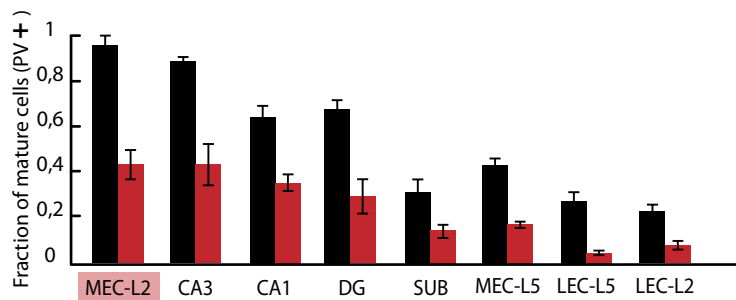
Fig. S4

A

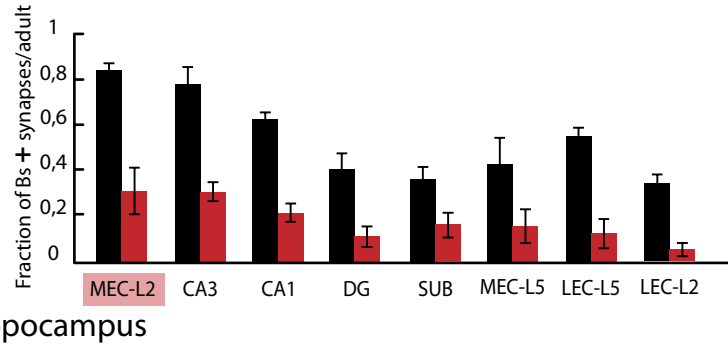


Silencing of MEC-L2

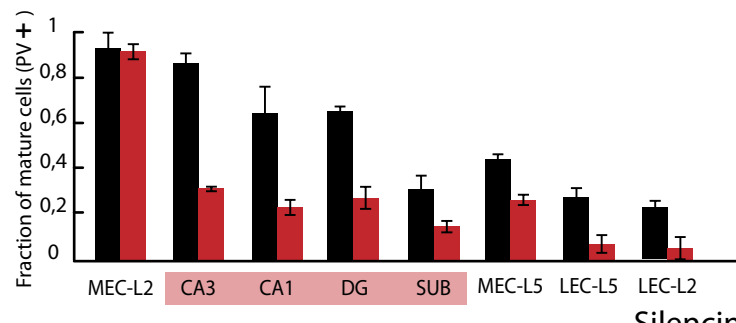
B



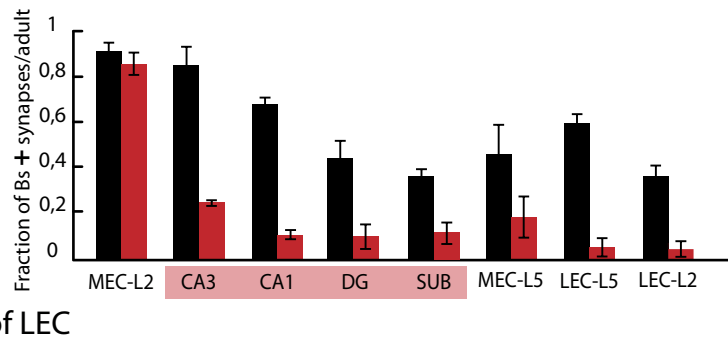
C



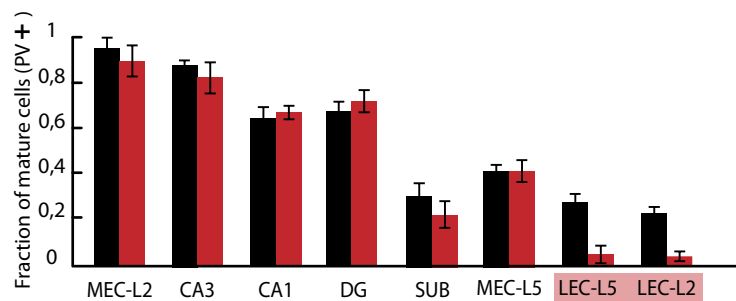
D



E



F



G

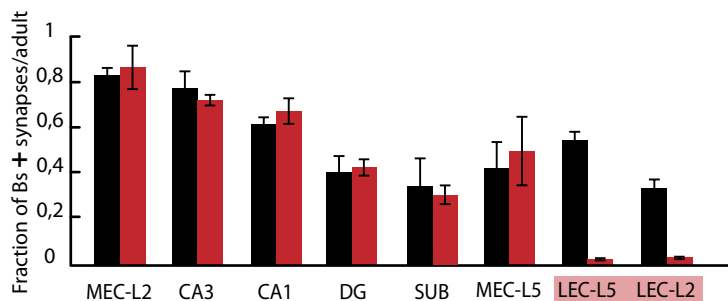


Fig. S4: PV expression and synaptic density upon developmental silencing of particular subregions of the entorhinal-hippocampal network.

(A) Upper pair of rows: confocal images showing DCX expression (white) across subregions of the entorhinal-hippocampal circuit. Upper row: control animals. Lower row: same regions after silencing MEC-L2 excitatory neurons for 6 days. Image locations are indicated in Fig. S1A. Single fields of view were acquired with a $40\times/1.3\text{NA}$ oil immersion objective (zoom $0.6\times$), and processed together, with constant parameters. Lower pair of rows: processed dataset. Individual neurons (identified automatically based on the expression of somatic markers, as in Fig. S1C) have been labelled as regions of interest (ROI), and each individual ROI has been hand-drawn onto the maximum intensity projection of the DCX signal across the 3D dataset. Single ROIs (solid circles) are colour-coded based on presence (magenta) or absence (white) of DCX, as in Fig. S1C. Note that the overall level of fluorescence present in specific regions of an image (hippocampus), or diffused through the whole extent of the cell layer (cortex), can be the result of neuropil contamination, which has been excluded from our single-cell analysis as previously explained (Fig. S1C). Above each image its proportion of DCX- cells, compared to the mean value across animals (left and right of slash, respectively; means as in Fig. 2A) is indicated. (B)-(G). Individual panels show local fractions of PV+ cells (B, D, F) and bassoon labelled synaptic puncta (Bs+; C, E, G) at P20 in different parts of the entorhinal-hippocampal circuit. Both PV+ and Bs+ numbers are normalized to counts from adult animals (P90). x axis: Local network under investigation. Areas highlighted in red on the x axis-label indicate silenced regions. (B) MEC-L2-specific silencing prevented maturation-related increase in PV expression throughout the entorhinal-hippocampal network (> 15000 neurons analyzed from at least 3 animals per experimental group; mean \pm S.D., silenced vs. control: $t > 10.50$ and $P < 0.0001$). (C) MEC-L2-specific silencing prevented maturation-related increase in density of synaptic puncta throughout the entorhinal-hippocampal network.(mean \pm S.D., $t > 8.463$ and $P < 0.0001$). (D) Hippocampus-specific silencing did not affect PV expression in MEC-L2, but affected the rest of the network ($t = 0.18$ and $P = 0.1$ for MEC-L2, $t > 10.1$ and $P < 0.0001$ for all other comparisons; > 15000 neurons analyzed from at least 3 animals per experimental group). (E) Hippocampus-specific silencing did not affect synaptic densities in MEC-L2, but reduced densities in the rest of the network ($t = 0.20$ and $P = 0.80$ for MEC-L2, $t > 8.5$ and $P < 0.0001$ for all other comparisons). (F) LEC-specific silencing affected PV expression only in LEC-L5 and LEC-L2 ($t > 5.1$ and $P < 0.0001$ for the LEC, $t < 0.95$ and $P > 0.2$ for all other comparisons; > 15000 neurons analyzed from at least 3 animals per experimental group). (G)

LEC-specific silencing affected synaptic densities only in LEC-L5 and LEC-L2 ($t > 8.1$ and $P < 0.0001$ for the LEC, $t < 1.5$ and $P > 0.52$ for all other comparisons).

Fig. S5

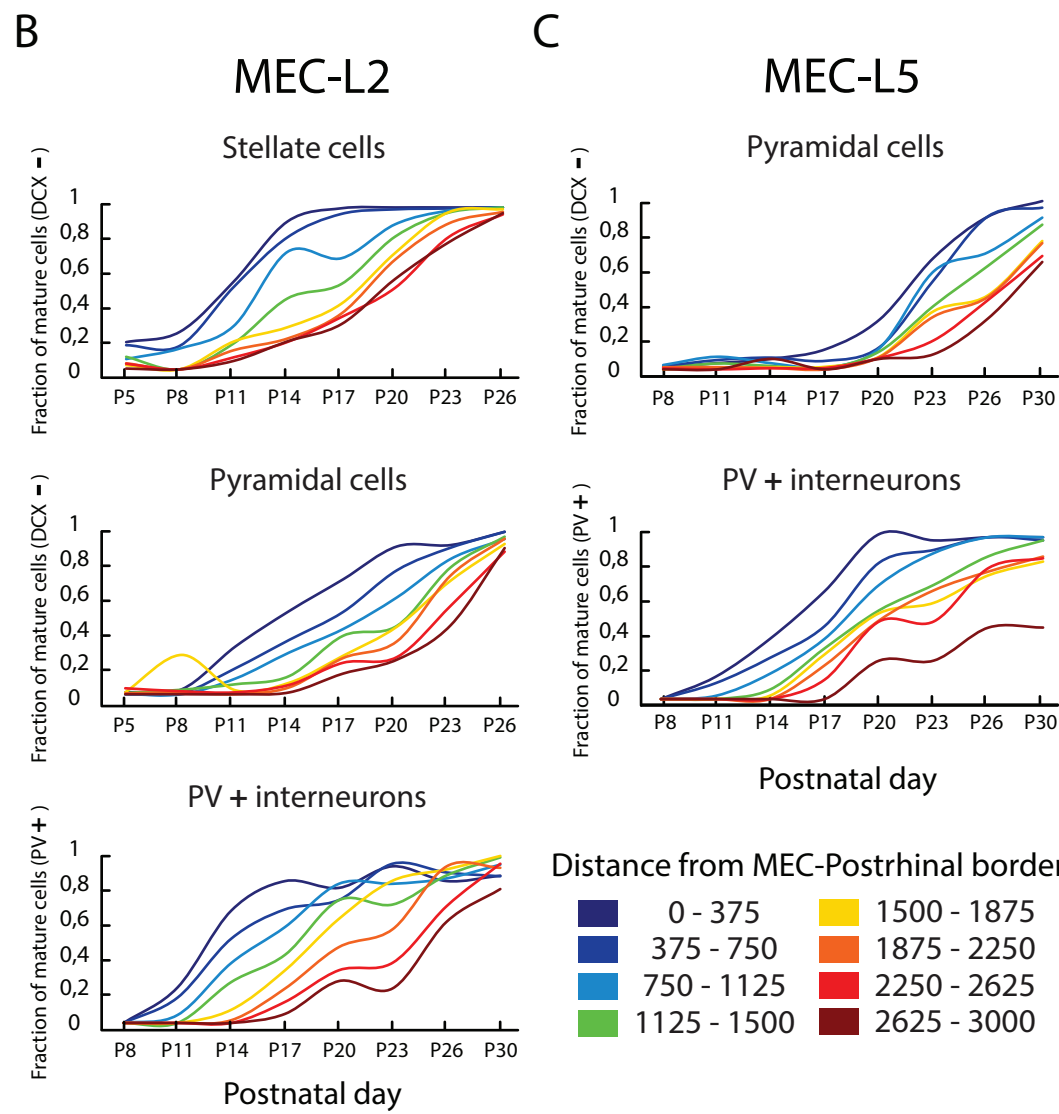
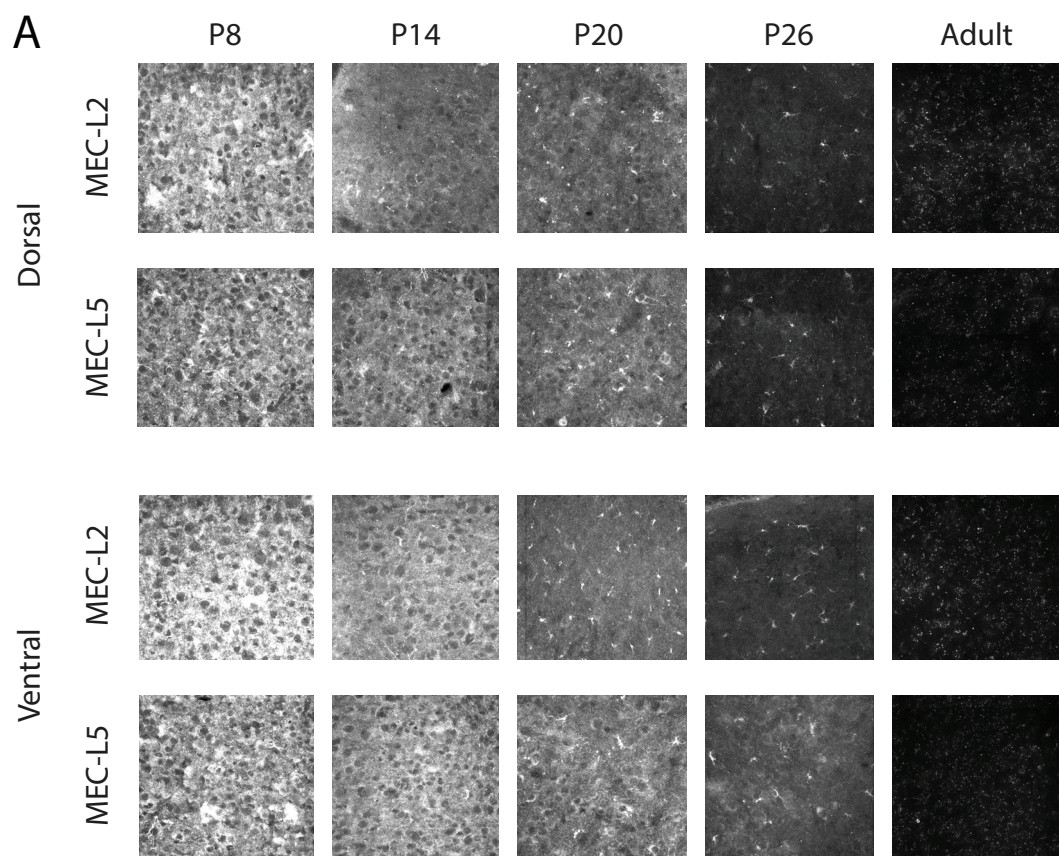


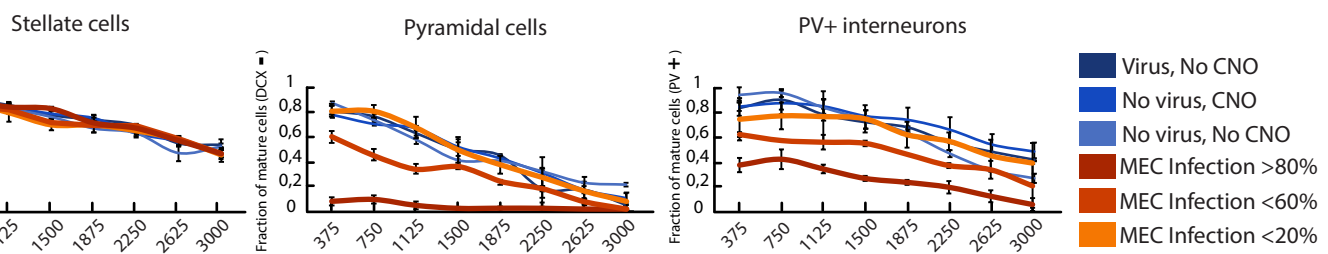
Fig. S5: Dorso-ventral topography of MEC maturation.

(A) Confocal images showing DCX expression (white) in dorsal and ventral MEC at multiple time points during the first postnatal month (image locations indicated in Fig S1B; dorsal and ventral MEC analyzed at the same medio-lateral location). Single fields of views were acquired with a $40\times/1.3\text{NA}$ oil immersion objective (zoom $0.6\times$), and processed together, with constant parameters.

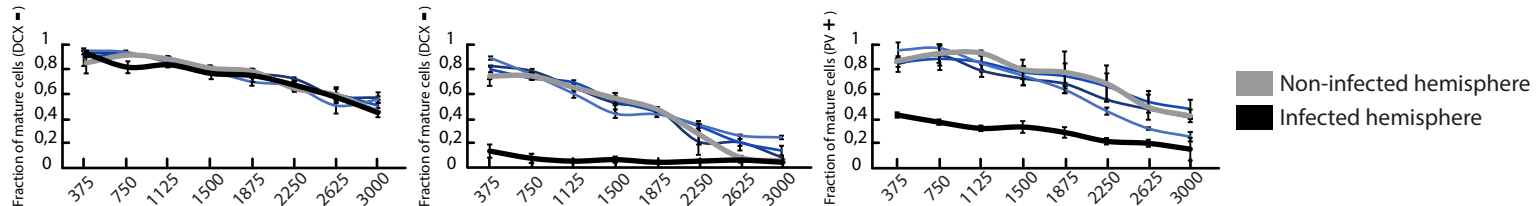
(B) Dorso-ventral topography of maturation in MEC-L2 (B) and MEC-L5 (C). Cumulative distributions are colour coded by location along the dorso-ventral axis of the MEC, from dorsal (blue) to ventral (red), with 0 set at the border between postrhinal and entorhinal cortex. *x* axis: day after birth. Upper panel: cumulative distributions of DCX⁻ stellate cells. *y* axis: local fraction of reelin+ cells expressing DCX below detection level. 0: All cells express DCX. 1: No cells express DCX. 2-way ANOVA with Group and Segment as factors (Group \times Segment: $F(7, 32) > 29.3$, $P < 0.0001$). The comparison between the first and second location was not significant, Group \times Segment: $F(7, 32) = 0.98$, $P = 0.72$). Middle panel: cumulative distributions of DCX⁻ pyramidal cells. *y* axis: local fraction of calbindin+ cells expressing DCX below detection level. 0: All cells express DCX. 1: No cells express DCX. Group \times Segment: $F(7, 32) = 62.4$, $P < 0.0001$). Lower panel: cumulative distributions of PV+ neurons normalized to the adult network (P90-120). *y* axis: local fraction of PV+ network expressing PV at the time of analysis. 0: No cell expresses PV. 1: All cells express PV. (Group \times Segment: $F(7, 32) = 43.6$, $P < 0.0001$). (C) Dorso-ventral topography of MEC-L5 maturation. Upper panel: cumulative distributions of DCX⁻, NeuN+ cells. *y* axis: local fraction of NeuN+ cells expressing DCX below detection level. 0: All cells express DCX. 1: No cells express DCX. *x* axis: day after birth. Color codes describe location along the dorso-ventral axis of the MEC, from dorsal (blue) to ventral (red). 0 is set at the border between postrhinal and entorhinal cortex. Group \times Segment: $F(7, 32) = 32.4$, $P < 0.001$). Lower panel: cumulative distributions of PV+ neurons normalized by the adult network (P90-120). *y* axis: local fraction of the adult PV+ network expressing PV at the time of the analysis. 0: No cell expresses PV. 1: All cells express PV. *x* axis: day after birth. Color code as in (A). Group \times Segment: $F(7, 32) = 52.7$, $P < 0.0001$.

Fig. S6

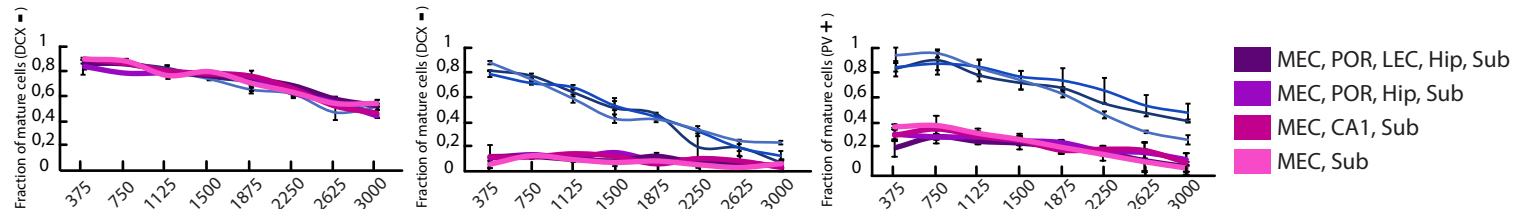
A



B



C



D

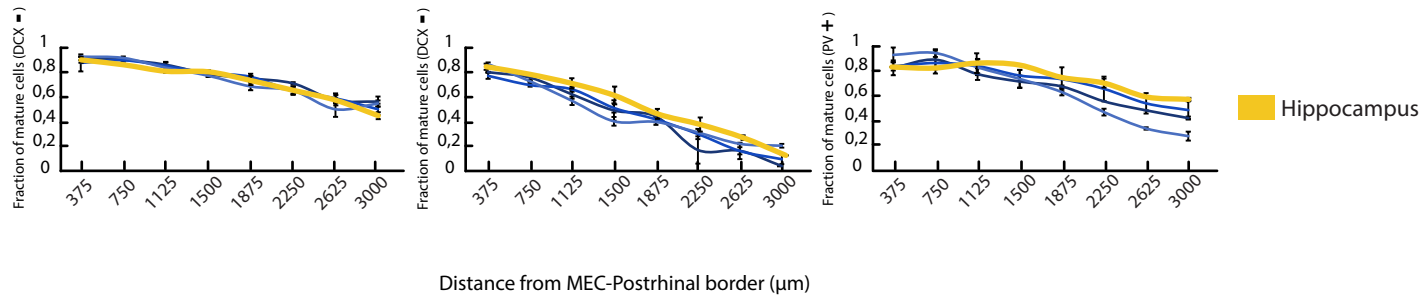


Fig. S6: Local analysis of maturation in MEC-L2 excitatory and inhibitory neurons upon developmental silencing.

(A) Effect of silencing MEC-L2 on network maturation as a function of the fraction of neurons silenced. The fraction of DCX– pyramidal cells and PV+ interneurons was reduced in proportion to the fraction of neurons infected. Values in control animals were from three categorically different groups: (i) No virus, No CNO; (ii) Virus, No CNO; (iii) No Virus, CNO (different shades of blue). DCX–fractions ranged from 0.06 to 0 when more than 80% of the excitatory cells of MEC-L2 were silenced (2-way ANOVA with Group and Segment as factors, every combination of >80% silencing vs. control groups: $F(7, 32) > 10.6$ and $P < 0.0001$, in agreement with Fig. 3B). Fractions ranged from 0.60 to 0 when the proportion of MEC-L2 neurons silenced was between 20 and 60% (Group \times Segment: $F(7, 32) > 4.7$ and $P < 0.01$), and from 0.83 to 0.07 when less than 20% of MEC-L2 neurons were silenced (Group \times Segment: $F(7, 32) < 1.3$ and $P > 0.4$). Values for PV+ neurons ranged from 0.98 to 0.42 along the dorso-ventral MEC axis for controls, from 0.43 to 0.07 when more than 80% of the excitatory cells of MEC-L2 were silenced (Group \times Segment: $F(7, 32) > 7.9$ and $P < 0.0001$, in agreement with Fig. 3B), from 0.70 to 0.24 when the proportion of neurons silenced ranged from 20 to 60% (Group \times Segment: $F(7, 32) > 6.9$ and $P < 0.001$), and from 0.86 to 0.45 when less than 20% of neurons were silenced in MEC-L2 (Group \times Segment: $F(7, 32) < 2.01$ and $P > 0.2$). For stellate cells, none of the silencing groups were different from controls (in agreement with Fig. 3B, Group \times Segment: $F(7, 32) < 1.84$ and $P > 0.23$). **(B)** Silencing MEC of its homotopic contralateral inputs, which mainly come from pyramidal cells in layer 3 (14, 56), does not influence maturation of the layer2 network. Curves refer to animals in which only one hemisphere was infected by the DREADD virus, while the other was clear of infected cells ($< 0.1 \pm 0.005\%$). In the infected group, hM4D(Gi) expression was visible across layers (L2 to L5) but specific to MEC. Stellate cells (left panel), pyramidal cells (central panel) and PV+ interneurons (right panel) do not exhibit any delay in maturation of the contralateral hemisphere as a consequence of silencing (light grey curves) when compared to control animals (2-way ANOVA, Group \times Segment: $F(7, 32) < 1.03$, $P > 0.23$). Note that the fraction of DCX– stellate and pyramidal cells and PV+ neurons is not different from that found in control animals in the contralateral hemisphere of infected animals. In the ipsilateral hemisphere, pyramidal cells and PV+ neurons, but not stellate cells, exhibited delays in maturation when compared to control animals (black, multiple comparisons between every combination of stellate, pyramidal cell and interneurons from silenced groups and their controls: Group \times Segment: $F(7, 32) > 7.3$ and

$P < 0.001$ for pyramidal cells and PV+ neurons; Group \times Segment: $F(7, 32)$: $F = 0.9$ and $P = 0.8$ for stellate cells). **(C)** Silencing an extensive part of the retrohippocampal area did not affect maturation of stellate cells but blocked maturation of pyramidal cells and PV+ neurons. Retrohippocampal silenced mice were split into three groups according to the spread of infection in the retrohippocampal areas (figure legend, different shades of purple). MEC layers 2 and 5 were silenced in all groups but the infection also extended into postrhinal cortex, lateral entorhinal cortex, hippocampus and subiculum in different groups. Values of DCX– pyramidal cells ranged from 0.85 to 0.11 along the dorso-ventral axis of the MEC for controls, but only from 0.04 to 0.02 when a large retrohippocampal region was silenced (Group \times Segment: $F(7, 32) > 20.984$ and $P < 0.0001$). Values for PV+ neurons ranged from 0.98 to 0.42 along the dorso-ventral MEC for controls and from 0.40 to 0.02 when a large retrohippocampal region was silenced (Group \times Segment: $F(7, 32) > 10.7$ and $P < 0.0001$). Stellate cells did not exhibit any differences from controls for any group of retrohippocampal silenced animals (Group \times Segment: $F(7, 32) > 2.3$, $P > 0.07$). Data are from > 250000 neurons of > 30 animals, with at least 3 hemispheres for each condition. **(D)** Stellate cell, pyramidal cell and PV+ neuron maturation was not affected at any position along the dorso-ventral MEC axis when excitatory neurons in the hippocampus were silenced. Values were indistinguishable from controls for both DCX expression in stellate and pyramidal cells and for PV expression in interneurons (2-way ANOVA, Group: $F(1, 32) < 2.60$ and $P > 0.28$; Group \times Segment: $F(7, 32) < 0.94$ and $P > 0.65$).

Fig. S7

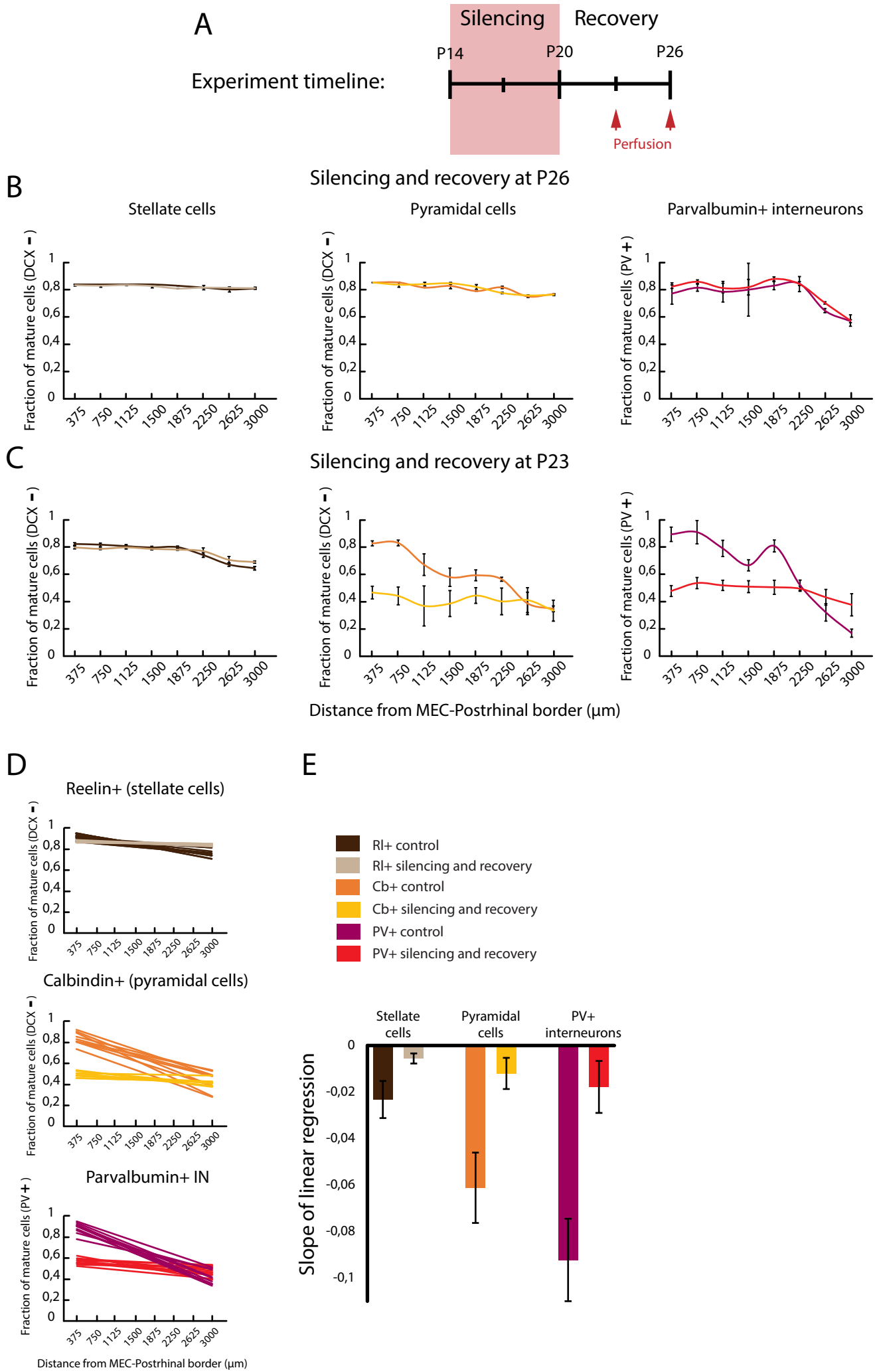
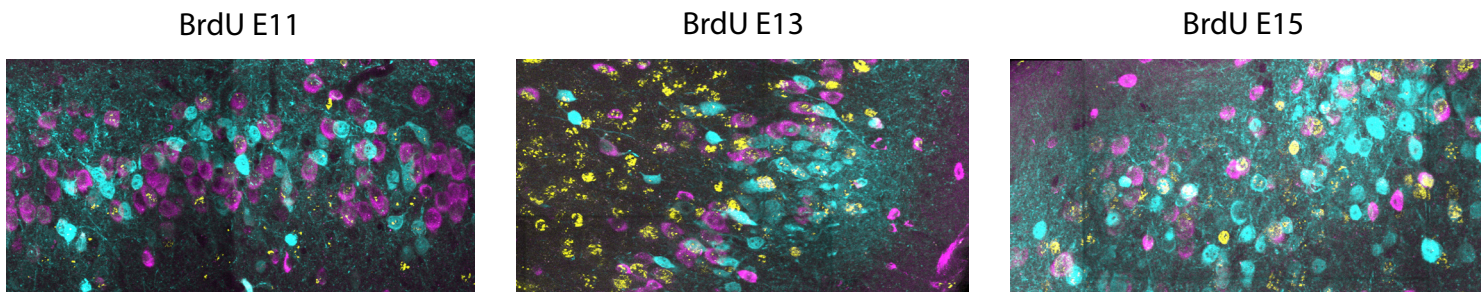


Fig. S7: Developmental silencing does not result in long-term impairment of MEC-L2 network maturation.

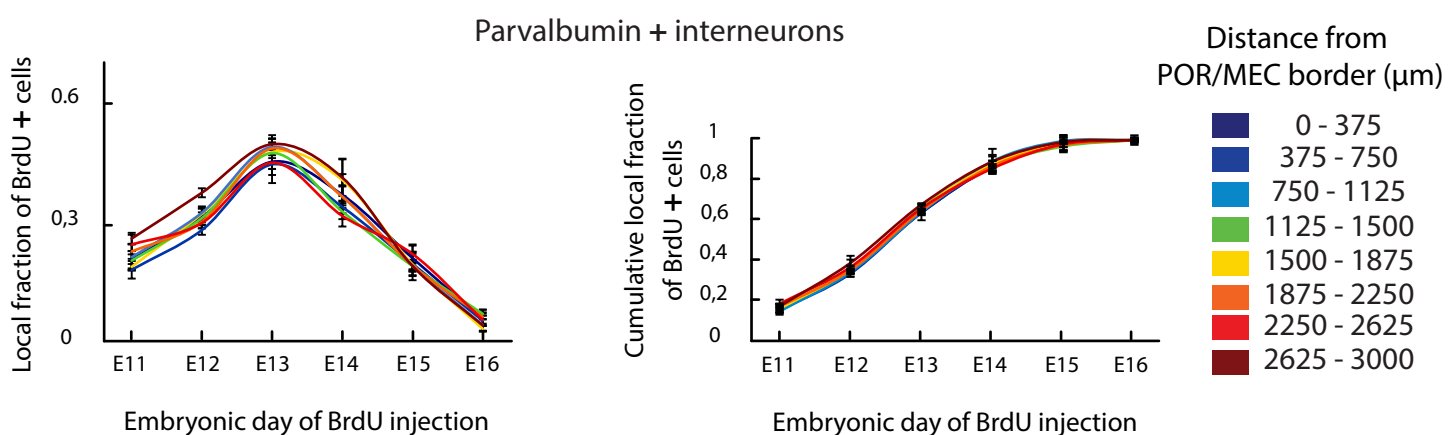
(A) To test if local silencing causes lasting damage to the network, as opposed to only delaying its maturation, we allowed a cohort of mice to recover after removal of the minipump at P20. We analyzed subsequent network maturation at two time points: P23 and P26 (red arrows). **(B)** After 6 days of recovery, at P26, DCX and PV expression levels were comparable to control animals (P26 cohort, comparison between silenced and control animals for DCX expression in pyramidal cells and PV expression in interneurons did not yield any significant difference, Group \times Segment: $F(7, 32) < 0.51$, $P > 0.10$). **(C)** At P23, the fraction of DCX $^-$ pyramidal cells and PV $^+$ interneurons was still significantly different from that of time-matched controls (No virus, Saline) at every level along the dorso-ventral axis of MEC (comparisons between pyramidal cells or interneurons and their controls: Group \times Segment: $F(7, 32) > 7.23$, $P < 0.03$). However, fractions at P23 were also significantly different from values exhibited by silenced animals immediately after silencing at P20 (Fig. 3C and Fig. S6, pyramidal cells or interneurons vs. silenced animals: Group \times Segment: $F(7, 32) > 4.02$ and $P < 0.01$). The findings indicate that the network was able to recover normally after silencing, and that no long-term impairment in maturation had been caused by silencing excitatory activity during development. Stellate cells were not affected by silencing at any time during recovery (all combinations of comparisons among different time points of recovery and their controls: Group \times Segment: $F(7, 32) < 0.953$ and $P > 0.87$, (B) and (C) left panels). **(D)** Fraction of DCX $^-$ stellate cells (upper panel) and pyramidal cells (central panel), and PV expression in PV $^+$ neurons (lower panel), in single sagittal sections from recovering mice at P23 (lighter colors) or time-matched control animals (darker colors). Each line represents the linear regression through the values calculated on a single sagittal slice. Note lack of dorso-ventral MEC gradient for DCX $^-$ pyramidal cells and PV $^+$ interneurons, in contrast to control animals. For pyramidal cells, values in control animals ranged from 0.89 to 0.44 while they ranged from only 0.55 to 0.47 in recovering animals, suggesting minimal dorsal-to-ventral difference in the recovery group. Similarly, for PV $^+$ cells, values ranged from 0.87 to 0.51 in control animals, but ranged only from 0.58 to 0.49 in silenced animals. **(E)** The slope of the linear regressions in (D) was close to 0 in pyramidal and PV $^+$ cells of recovering animals at P23, indicating no topographical difference in maturation between dorsal and ventral MEC (Student's t-test, $t > 6.1$ and $P < 0.001$, mean \pm S.D.). No significant dorsal-to-ventral difference could be observed for stellate cells in D or E.

Fig. S8

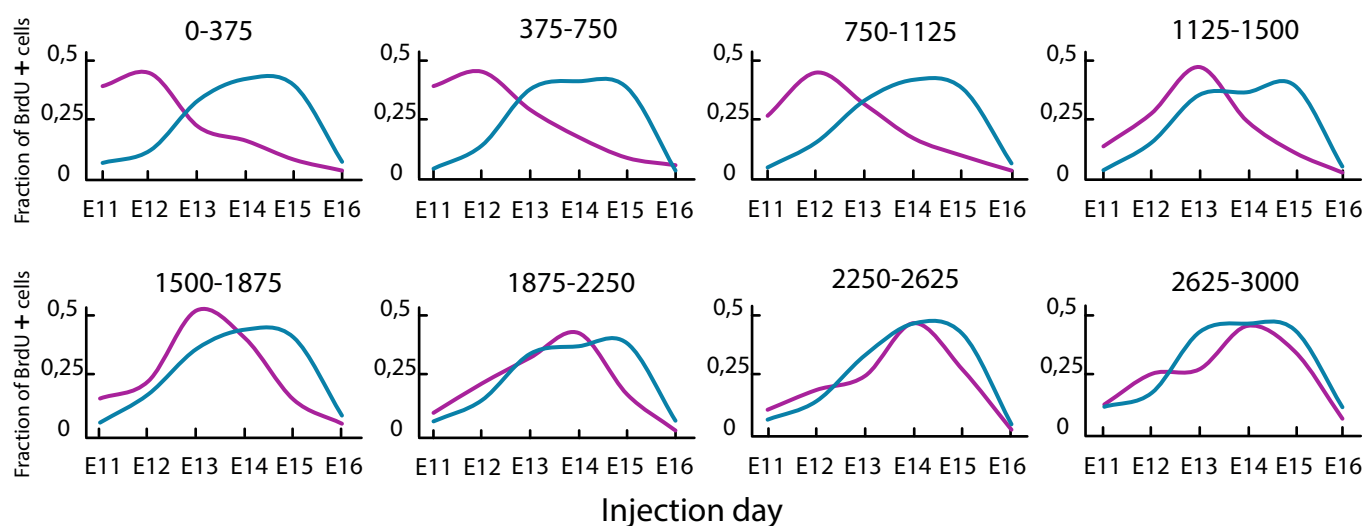
A



B



C



D

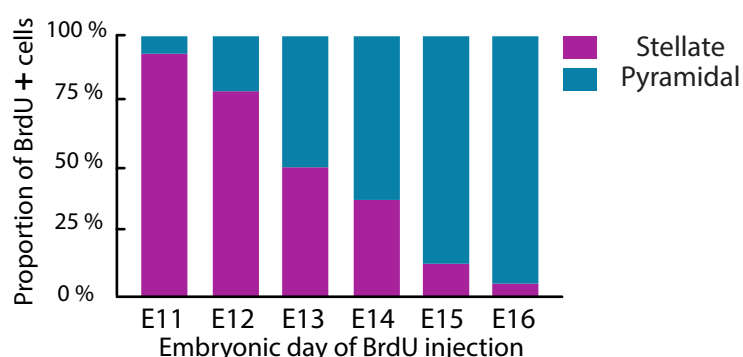


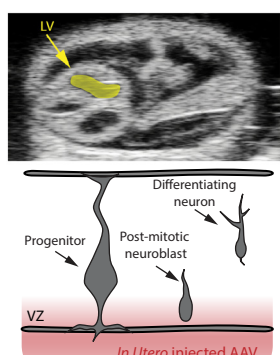
Fig. S8: No topography in neurogenesis of PV+ cells along dorso-ventral MEC axis.

(A) 20 \times confocal images of sagittal sections from animals injected with BrdU at three time points during embryonic development (cyan: calbindin; magenta: reelin; yellow: BrdU, maximum intensity projections). (B) Local density estimates of neurogenesis of PV+ cells. For each of the eight blocks along MEC (Fig. 3A), we quantified the number of neurons positive for PV, and analyzed the proportion of them that exhibited BrdU staining in the nucleus. Left panel: y axis: proportion of the PV+ network labelled with BrdU for each embryonic day when BrdU was injected (x axis). 0: no PV+ cells labelled with BrdU; 1: all PV+ cells labelled with BrdU). Local peak indicates peak of neurogenesis. > 250000 neurons from at least 3 mice per time point. Right panel: cumulative distributions of the fraction of PV+ neurons labelled by BrdU across injection days (mean \pm S.D.; same data as in left panel). Injection of BrdU at E10 and E17 did not produce any detectable staining in the adult, thereby marking the beginning and the end, respectively, of the MEC neurogenesis window. No staggering of curves indicates a homogenous distribution of neurogenesis along the dorso-ventral axis of MEC for PV+ cells (Injection day: F(2, 36) = 0.79, P = 0.43; Segment: F(7, 36) = 1.53, P = 0.68; Segment \times Injection Day: F(7, 36) = 0.15, P = 0.87). (C) Neurogenesis profiles of stellate and pyramidal cells at every dorso-ventral position of the MEC. The fraction of stellate or pyramidal cells labelled by BrdU (y axis) was plotted as a function of BrdU injection time during development (x axis) for every block of MEC analyzed (ranges at top of individual panels indicate distance in μ m from postrhinal/entorhinal border). Direct comparison of stellate and pyramidal cell neurogenesis at individual dorso-ventral levels revealed that stellate cells were consistently born before pyramidal cells in the dorsal half of the MEC. For pyramidal cells, the peak of neurogenesis occurred on E14 for every position along the dorso-ventral axis, while it varied from E12 to E14 for stellate cells because of their topographical distribution. (D) Bar diagram indicating the molecular identity of BrdU-labelled excitatory cells in MEC-L2 as a function of BrdU injection day. For all BrdU-labelled cells, we determined the expression of either reelin (stellate cells) or calbindin (pyramidal cells) with immunological methods, and calculated the proportions of the two classes of cells for every time point of BrdU injection. Note how cohorts of BrdU labelled neurons for earlier injections are dominated by stellate cells (96% of BrdU labelled cells at E11), while cohorts of BrdU labelled neurons for later injections are dominated by pyramidal cells (94% of neurons labelled at E16). The analysis was conducted on the most dorsal portion of the MEC (0-375 μ m from the border to the postrhinal cortex).

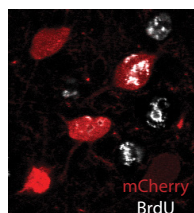
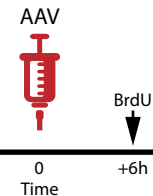
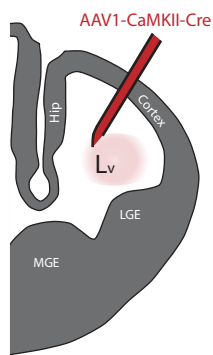
Fig. S9

A

In Utero injection

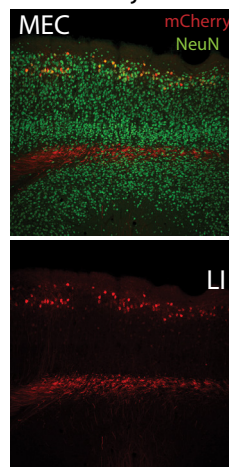


B

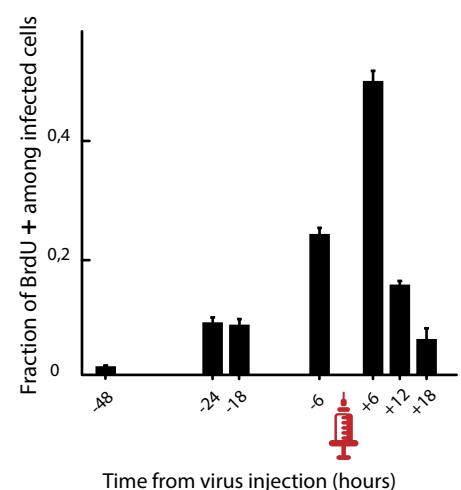


C

Adult injection

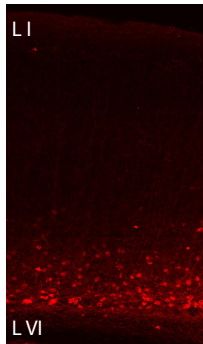


D

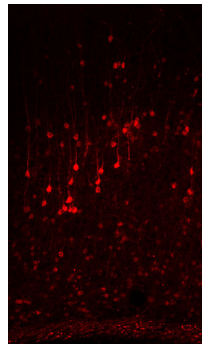


E

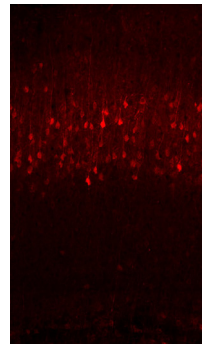
E12



E14



E16



F

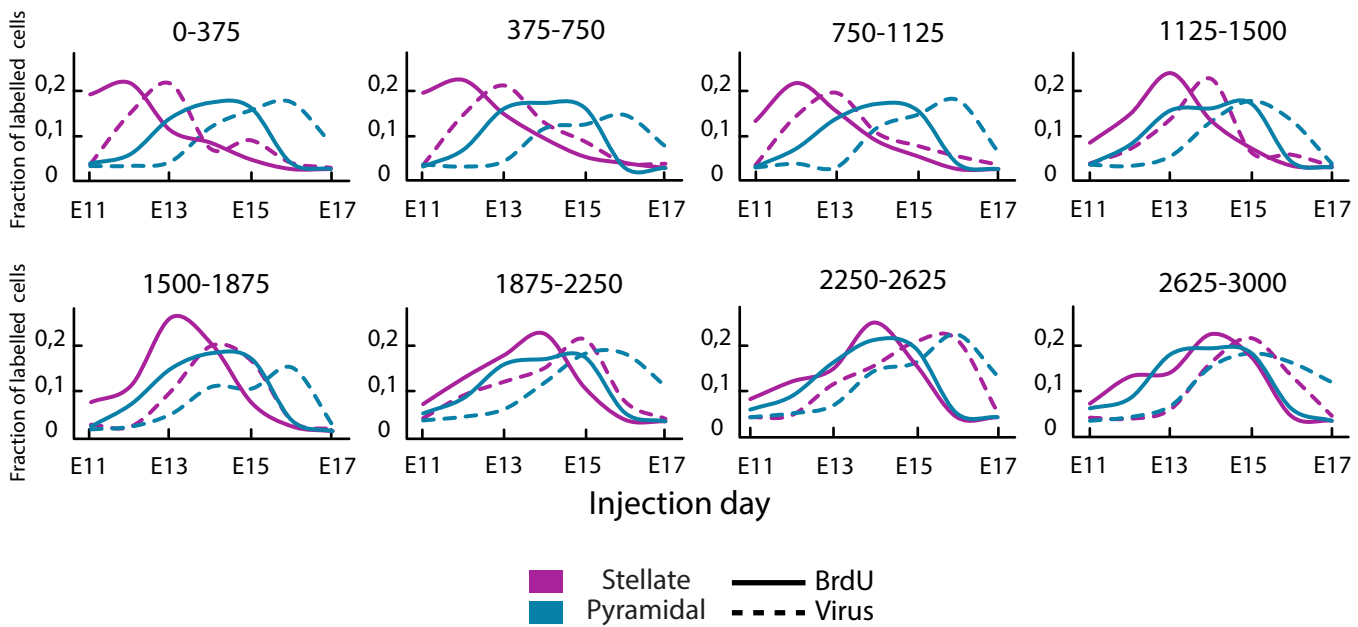


Fig. S9: Description and validation of method for genetic labelling of isochronic cohorts of neurons in the developing neocortex.

(A) Schematic illustrating key principles of the method. The temporal specificity of the genetic labelling is based on the deficiency of adeno-associated viral vectors to integrate into the genome of the infected cell, and on the transient permanence of post-mitotic neuroblasts in the ventricular zone (VZ) before migration. The viral construct does not integrate into the host genome, and hence the permanence of the viral genome at the episomal state should prevent inheritance of the viral construct by the progeny of infected progenitors (episomal DNA is effectively lost during cell division), while recycling of the cerebrospinal fluid should set a temporal limit for the action of the virus on progenitors and post-mitotic neuroblasts. Targeting the virus to the lateral ventricle (via ultrasound-guided injections, left upper and right panels) reduces the chances of infecting neuroblasts that have completed their final cell division before injection (and hence have migrated out of the ventricular zone, left lower panel), thereby setting a temporal limit for infection. **(B)** Double-labelling approach to verify the temporal specificity of viral labelling during development and to map the temporal extent of the neurogenesis window covered by viral injection. The pregnant mother was injected with BrdU either before or after viral injection of the embryos. Lower image: 40 \times maximum intensity projection, MEC-L2. White: immunodetection of BrdU; red: expression of mCherry as a consequence of viral infection. **(C)** A second viral injection (AAV1-CAG-Flex-mCherry) in the adult revealed developmentally labelled neurons in the MEC. Red, mCherry expressing neurons indicate neurons infected by the Cre virus during embryonic development, and by the FLEX-mCherry virus in the adult. Green: NeuN counterstaining. Note that a sparse number of neurons is labelled selectively in MEC-L2, as a consequence of the targeting of the virus and the time of infection during development. Red processes in deep layers represent axons projecting to the hippocampus. With this dual labelling approach, we first confirmed that our developmental viral infection was indeed effective in targeting a sparse population of cells, and that the proportion of labelled cells was constant during ageing across a period of 1 year. The infected fraction of cells in MEC-L2 after an injection at E13 was $21.4 \pm 7\%$ at 70 days post-injection, $20.8 \pm 7\%$ at 186 days post-injection and $23.1 \pm 10\%$ at 366 days post injection (Student's t-test, $t < 0.57$ and $P > 0.4$). The consistency of the number of labelled cells across days post injection rules out possible toxicity effects due to long-term permanence of the virus in the developmentally infected cells. **(D)** Fraction of mCherry-expressing cells that also stain for BrdU plotted as a function of temporal distance between BrdU and virus injection (y axis:

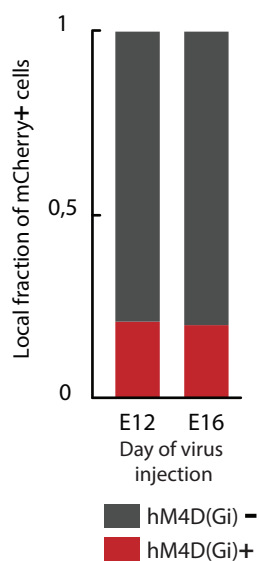
fraction of mCherry positive neurons labelled by BrdU at every time of BrdU injection. *x* axis: temporal distance between BrdU and *in utero* viral injection. 0 represents the time of viral injection. Values to the left of 0 represent time points when BrdU was injected before the virus; values to the right represent time points when BrdU was injected after the virus. Mean \pm S.D.) The bell-shape appearance of the double-labelling time course confirmed that viral labelling was largely confined to neurons whose cell division happened in a window of 24-32 hours around and after the time of viral injection (note that, for comparable time points of injection, over 80% of the virally-targeted population was born with a 6-28 hour lag in comparison to BrdU-labelled neurons). Thus, the viral method is effective in labelling isochronic populations of cortical neurons. (E) 10 \times low magnification images of visual cortex from mice injected in the embryo at different times during cortical neurogenesis (E12, E14 and E16). Images display maximum intensity projections of sagittal sections located 1.56 mm lateral to bregma. Mice were first injected with AAV1-CaMKII-Cre in the lateral ventricle during the embryonic stage, then with AAV1-CAG-Flex-mCherry in the adult cortex (P90-180). mCherry signal in red. Note that labelled cells follow the characteristic inside-out progression of cortical neurogenesis (30, 31), validating the viral labelling method as a tool for specific labelling of isochronic cohorts. Labelling at E12 targeted selectively cells in the deepest layers of cortex (left panel). Labelling at E14 targeted predominantly layer 4, in addition to significant populations of deep and superficial layers (central panel). Labelling at E16 targeted almost exclusively superficial layers (right panel). (F) To further validate the *in utero* viral method, and to verify that the topographic distribution of stellate cells by neurogenesis was not an artifact of the BrdU labelling method, we analyzed the spatio-temporal distribution of virally labelled, isochronic stellate and pyramidal cells born at different times during neurogenesis, and compared these with results obtained with BrdU labelling. Each plot shows the distribution of stellate (magenta) and pyramidal cells (cyan) labelled by virus (dashed lines) or BrdU (solid lines) (*y* axis) as a function of the time of injection during gestation (*x* axis). Notice how solid and dotted lines follow the same trend at every position along the dorso-ventral MEC axis (ranges at the top of individual panels: distance from the postrhinal-entorhinal border in μ m), confirming the topographical distribution of stellate cells as indicated by the BrdU approach. We did not fail to notice the rightward shift in the viral labelling curves with respect to the BrdU curves, which we attribute to the different phases of the cell cycle targeted by the two methods (S phase for BrdU and postmitotic phase for the viral injection), as well as the different temporal resolutions of the two approaches (6 vs. 24 hours, respectively).

Fig. S10

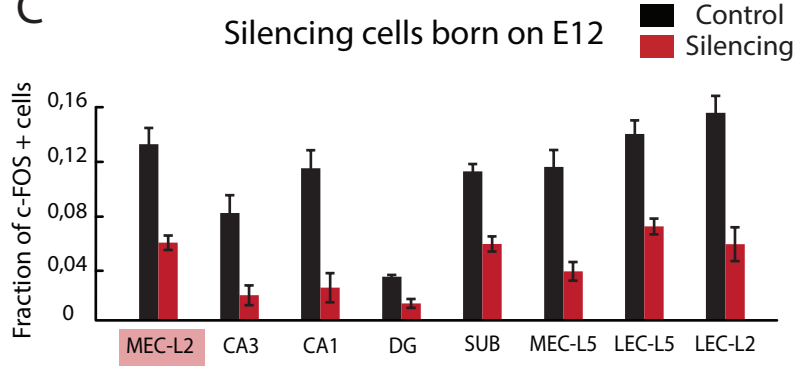
A



B



C



D

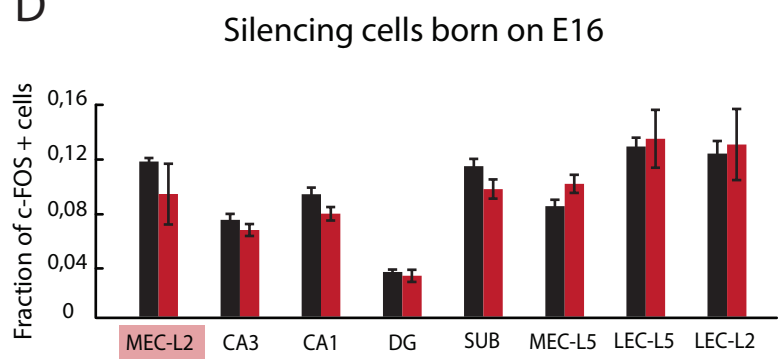


Fig. S10: Selective silencing of stellate or pyramidal cells in MEC-L2.

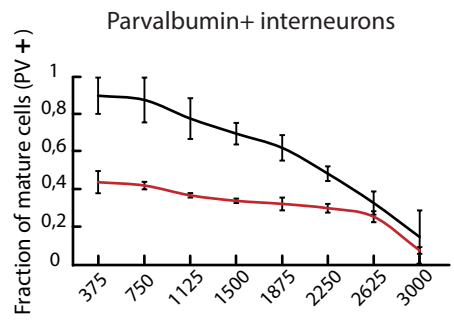
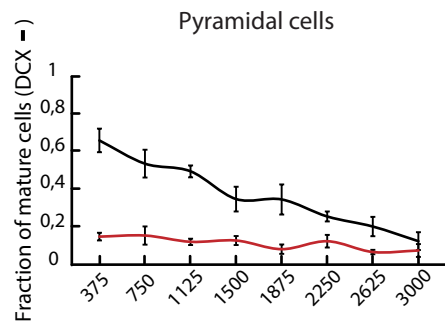
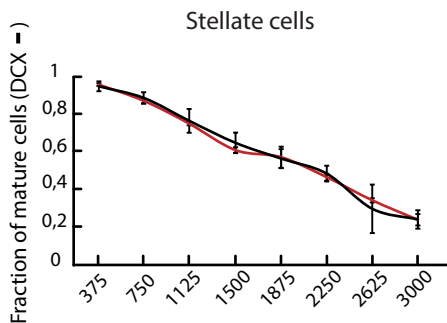
(A) Isochronic cohorts of neurons labelled by injection of the virus early during neurogenesis (E12) are dominated by stellate cells, which constitute $96 \pm 3\%$ of the infected neurons (upper pie chart), while isochronic cohorts of neurons labelled late during neurogenesis (E16) are dominated by pyramidal neurons, which constitute $92 \pm 4\%$ of the infected neurons (lower pie chart). Magenta: virally infected cells expressing reelin; cyan: virally infected cells expressing calbindin. **(B)** Fraction of the local network of excitatory cells in MEC-L2 expressing mCherry as a consequence of infection by AAV2-Syn-DIO-hM4D(Gi)-mCherry. Red bars: NeuN+ and mCherry+, Grey bars: NeuN+ and mCherry-. The fraction is $20 \pm 3\%$ for the animals injected at E12 and $18 \pm 4\%$ for animals injected at E16 (> 4000 cells from at least three animals for each injection group). **(C-D)** Fraction of NeuN+ neurons exhibiting nuclear expression of c-FOS (c-FOS+) across subdivisions of the entorhinal-hippocampal circuit in control animals (black) and silenced animals (red) (y axis: Fraction of double positive NeuN/c-FOS neurons. 0: no neurons express c-FOS; 1: all neurons express c-FOS). DREADD-mediated silencing induced a decrease in the fraction of c-FOS+ cells in the areas expressing the viral construct (x axis, red boxes) as well as areas downstream of the injected region only when isochronic neurons born on E12 were silenced (**C**, mean \pm S.D., Student's t-test comparisons to controls, $t > 9.42$ and $P < 0.001$) and not when the hM4D receptor targeted isochronic neurons born on E16 (**D**; $t < 2.72$ and $P > 0.58$).

Fig. S11

Control
Silencing

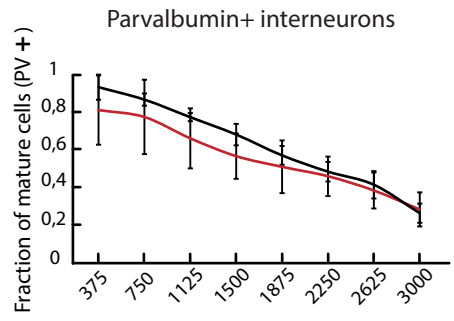
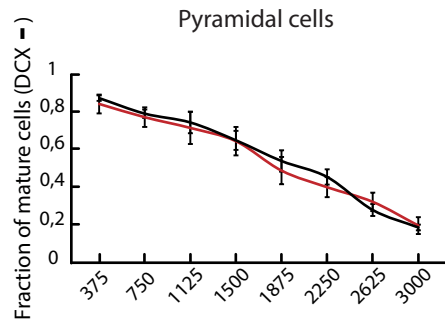
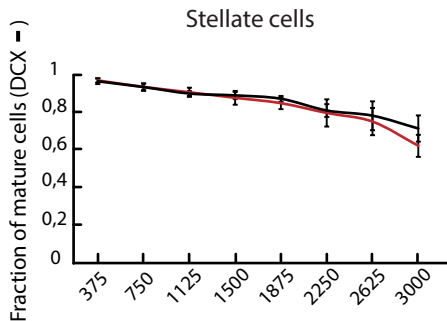
A

Labelling at E12, silencing during w1



B

Labelling at E12, silencing during w2



C

Labelling at E12, silencing during w3

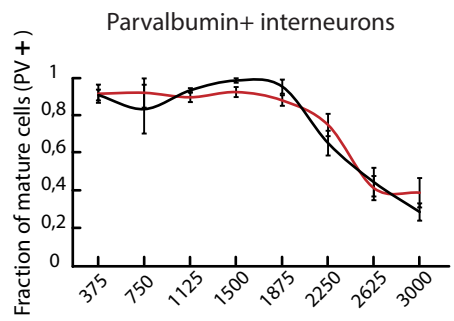
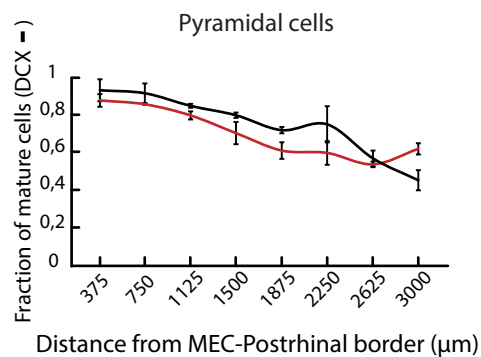
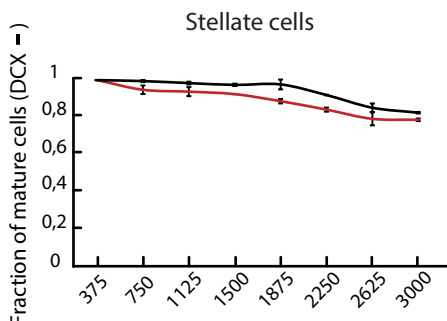


Fig. S11: Silencing stellate cells born on E12 blocks maturation in the local MEC-L2 network.

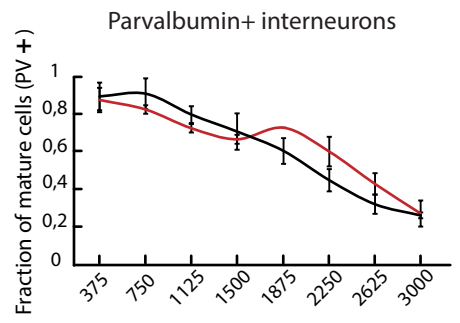
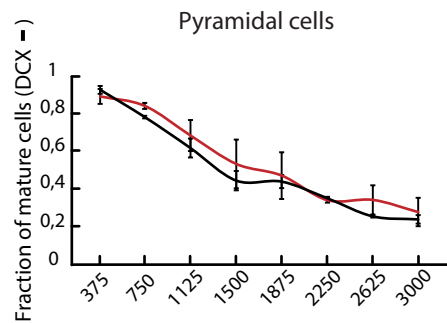
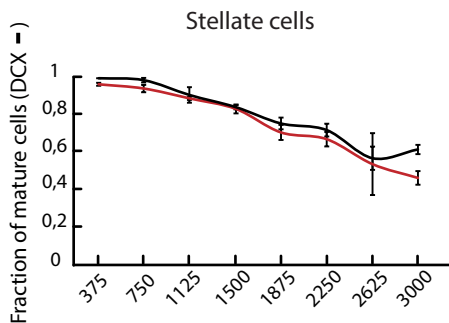
(A) Silencing stellate cells born at E12 during w1 (P14-P17) reduced the downregulation of DCX in pyramidal cells. The fraction of pyramidal cells with DCX expression below detection level ranged from 0.68 ± 0.07 (dorsal sector) to 0.11 ± 0.04 (ventral sector) in control animals (central panel, black line), and from only 0.14 ± 0.02 to 0.06 ± 0.04 in silenced animals (red line, Group \times Segment: $F(7, 32) = 83.90$, $P = 0.0001$). Right panel: silencing stellate cells born at E12 during w1 (P14-P17) prevented maturation-related increase in the fraction of interneurons expressing PV. The fraction of PV-expressing cells, normalized to adult levels, ranged from 0.89 ± 0.10 (dorsal sector) to 0.09 ± 0.09 (ventral sector) in controls, and from only 0.40 ± 0.06 to 0.01 ± 0.009 in silenced animals (Group \times Segment: $F(7, 32) = 64.2$, $P = 0.0001$). (B) and (C) No significant difference in DCX expression in pyramidal cells could be detected between silenced and control animals when CNO was delivered in a time-unmatched fashion during w2 (P17-P20, B; analysis at P20) or w3 (P20-P23, C; analysis at P23) (central panels, Group: $F(1, 32) < 2.97$ and $P > 0.12$; Group \times Segment: $F(7, 32) < 1.65$, $P > 0.54$). Similarly, there was no significant difference in PV expression between silenced and control animals when CNO was delivered in a time-unmatched fashion during w2 (P17-P20, B) or w3 (P20-P23, C) (right panels; Group: $F(1, 32) < 1.52$ and $P > 0.09$; Group \times Segment: $F(7, 32) < 2.12$, $P > 0.63$). Stellate cells were not affected by silencing when CNO was given in a time-matched fashion (A, left panel, Group: $F(1, 32) = 0.76$ and $P = 0.89$; Group \times Segment: $F(7, 32) = 2.30$, $P = 0.30$), or when silencing was offset from the normal maturation period (B and C, left panels, w2 vs. w3, Group: $F(1, 32) < 1.52$ and $P > 0.39$; Group \times Segment: $F(7, 32) < 1.62$ and $P > 0.47$).

Fig. S12

Control
Silencing

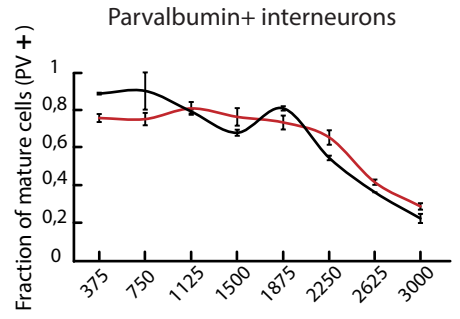
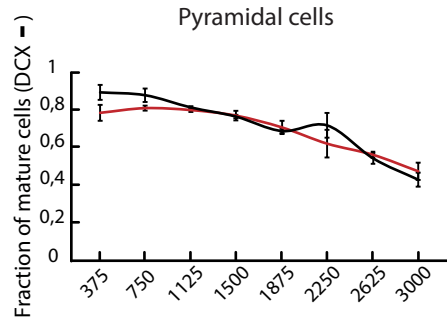
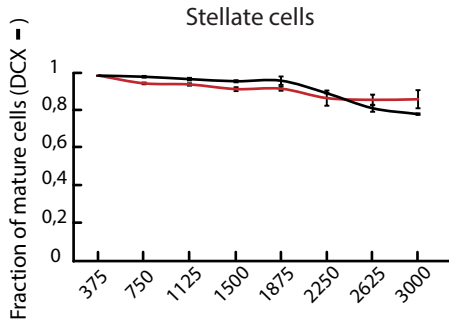
A

Labelling at E16, silencing during w2



B

Labelling at E16, silencing during w3



C

Labelling at E16, silencing during w4

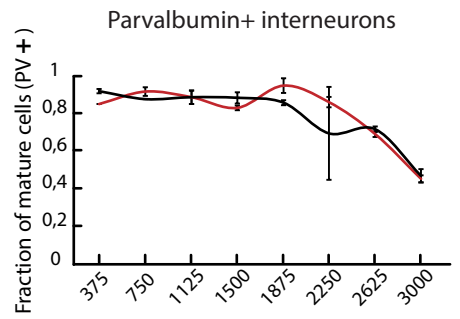
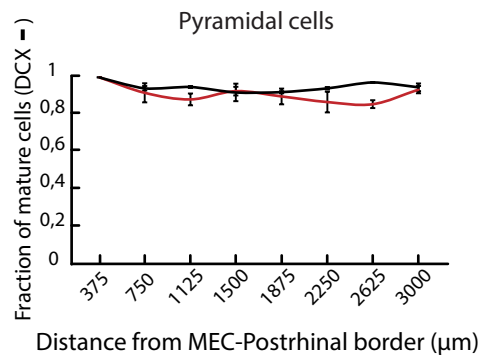
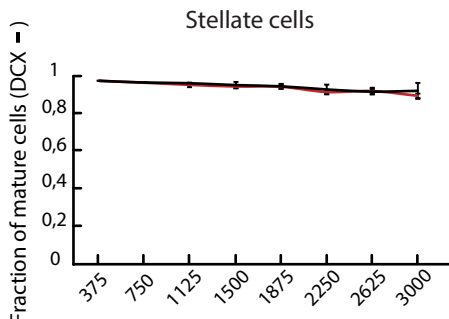


Fig. S12: Silencing pyramidal cells born on E16 does not affect maturation of the local MEC-L2 network.

(A), (B) and (C) Pyramidal cell-specific silencing did not affect maturation of the local MEC-L2 network. Silencing pyramidal neurons born at E16 produced no significant change in the expression of DCX in pyramidal cells (Group: $F(1, 32) < 3.68$ and $P > 0.08$; Group \times Segment: $F(7, 32) < 0.73$, $P > 0.51$) or stellate cells (Group: $F(1, 32) < 0.58$ and $P > 0.72$; Group \times Segment: $F(7, 32) < 0.98$, $P > 0.23$), or in the expression of PV in interneurons (Group: $F(1, 32) < 3.02$ and $P > 0.06$; Group \times Segment: $F(7, 32) < 1.04$, $P > 0.50$) (w2, w3 and w4 for CNO delivery in a time-unmatched and a time-matched fashion, respectively). Control animals are shown in black; silenced animals in red.

Fig. S13

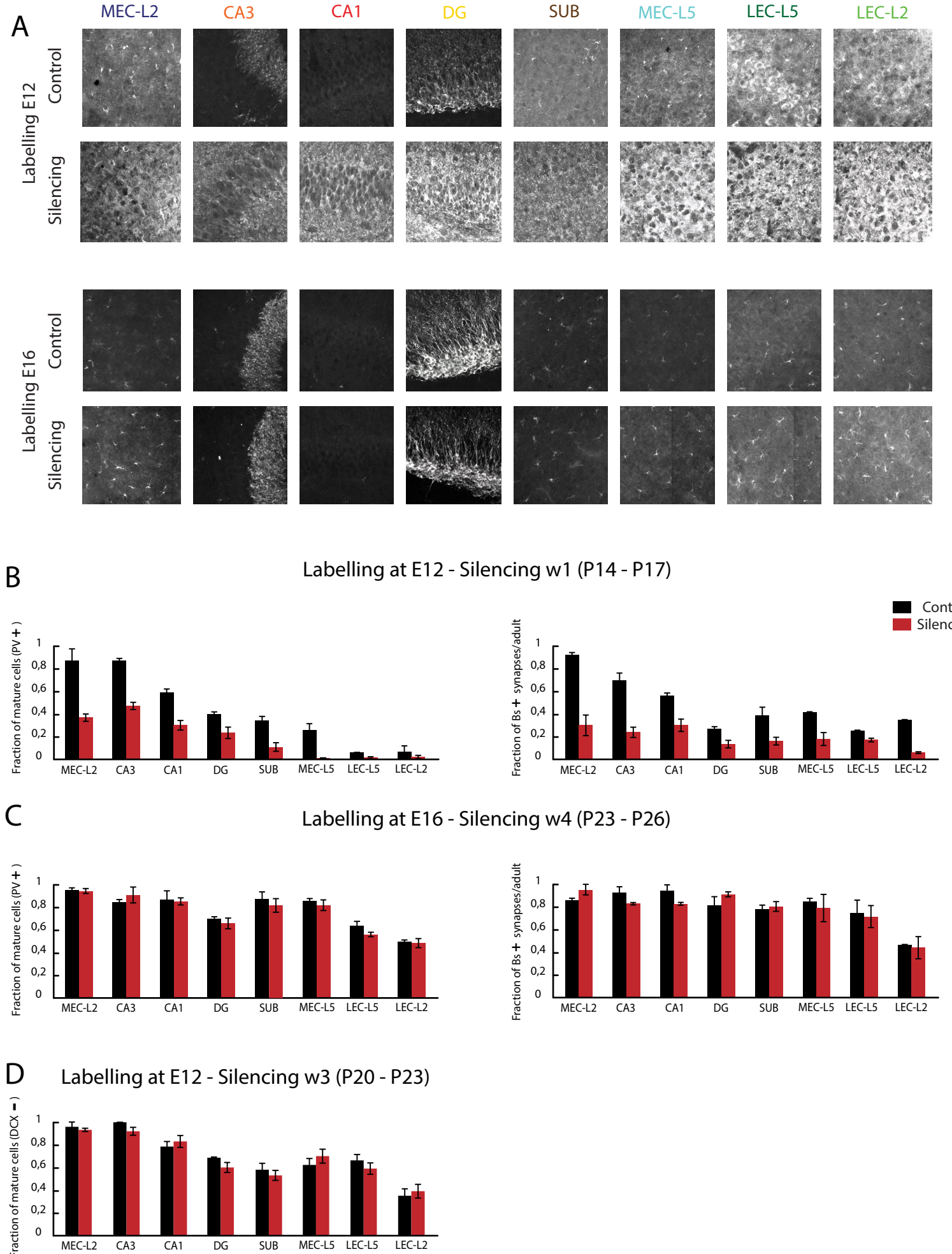


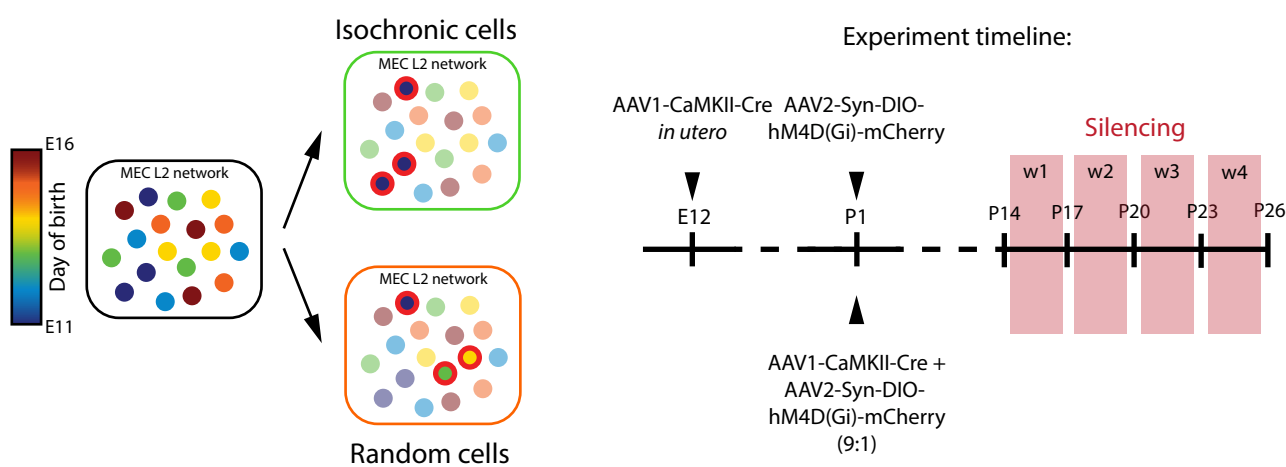
Fig. S13: PV expression and synaptic density after developmental silencing of either stellate or pyramidal cells.

(A) Maximum intensity projections from confocal images showing DCX expression (white) across subregions of the entorhinal-hippocampal circuit after selective silencing of stellate cells (upper 2 rows) or pyramidal cells (lower 2 rows). Single fields of view were acquired with a $40\times/1.3\text{NA}$ oil immersion objective (zoom $0.6\times$), and processed together with constant parameters. Note that silencing a small portion of stellate cells located in MEC-L2 was sufficient to induce an effect on the development of the extended circuit. This results rules out the possibility that the block of maturation caused by pharmacogenetic silencing might be due to cell-autonomous artifacts caused by the activation of the hM4D(gi) receptor in infected cells.

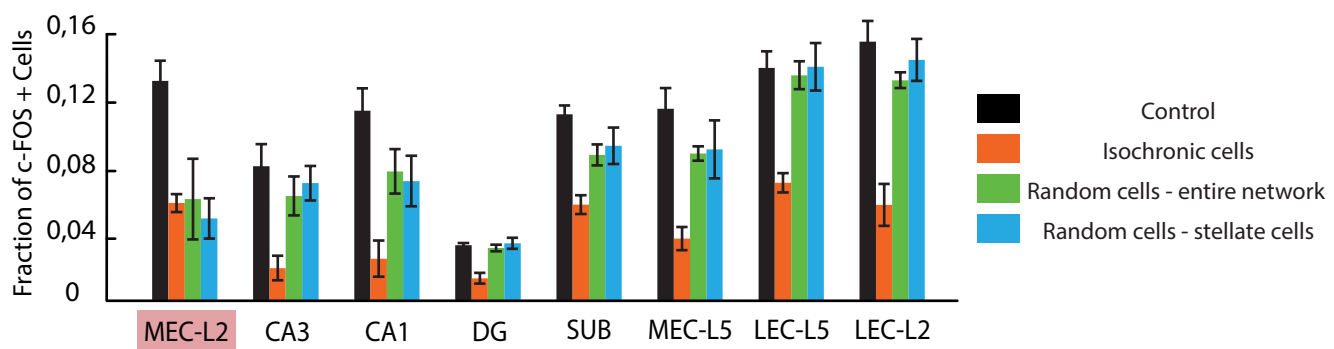
(B) Fraction of PV expressing cells (left) and density of bassoon puncta (right) across areas of the entorhinal-hippocampal network following silencing of E12-labelled neurons (predominantly stellate cells) at P14-P17. Analysis at P17. Stellate-cell specific silencing prevented the maturation-related increase in PV expression and synaptic densities across the whole entorhinal-hippocampal network. Silenced groups and control groups were compared with Student's t-test. PV cells: $t > 6.2$ and $P < 0.01$, with the exception of LEC-L5 and LEC-L2 where $t < 0.13$ and $P > 0.15$. Bs+ puncta: all pairwise comparisons with Student's t-test were significant ($t > 4.7$ and $P < 0.01$). **(C)** Fraction of PV expressing cells (left) and density of bassoon puncta (right) following silencing of E16-labelled neurons (predominantly pyramidal cells) at P23-P26. Analysis at P26. Silencing isochronic pyramidal cells did not exert any effect on maturation of the entorhinal-hippocampal network. Neither PV expression (left panel), nor densities of synaptic puncta (right panel) were different from controls in any area of the entorhinal-hippocampal network (no comparisons were significantly different, $t < 1.03$ and $P > 0.34$). **(D)** Fraction of DCX- cells upon silencing of isochronic cohorts dominated by stellate cells (E12-born; mean \pm S.D.). Cells were silenced at P20-P23 and analyzed at P23. DCX expression in silenced animals was indistinguishable from that of controls ($t < 2.41$ and $P > 0.72$), similarly to what was obtained along the dorso-ventral axis of MEC (Fig. S11C). Analysis was conducted with similar control groups and a similar number of neurons and animals as in (B).

Fig. S14

A

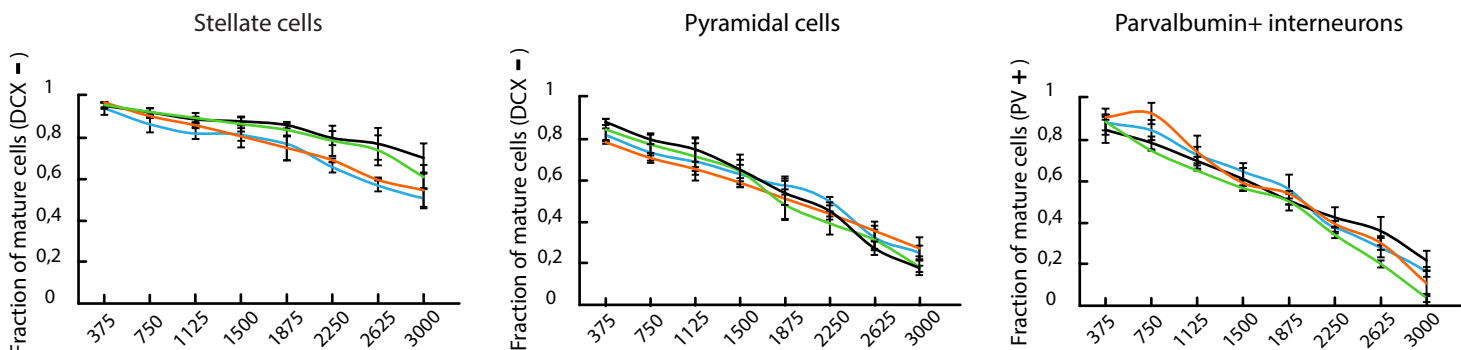


B



C

Silencing during w2



Silencing during w3

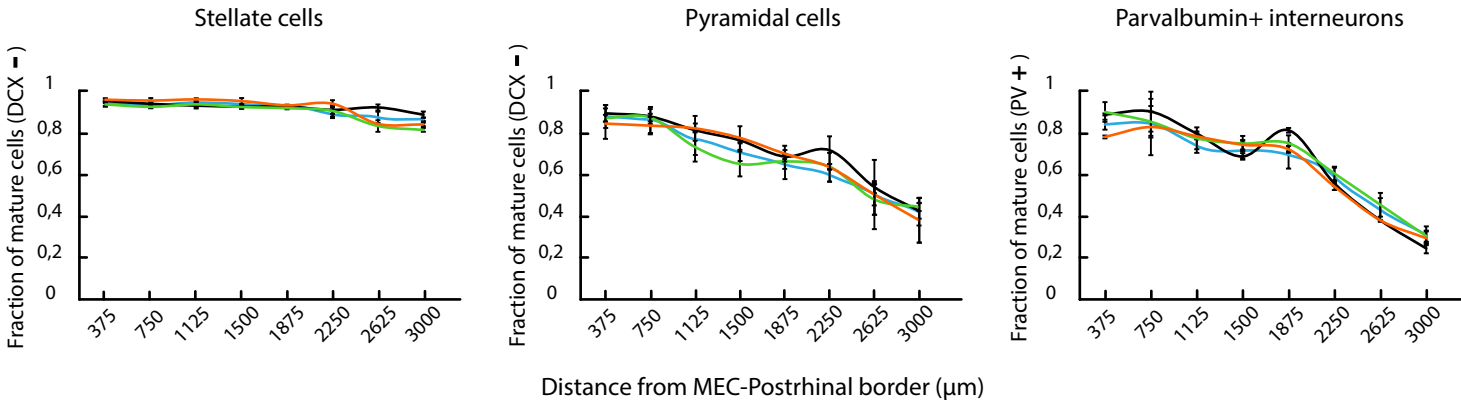


Fig. S14: Isochronic cohorts of stellate cells act synergistically on microcircuit maturation.

(A) Schematic illustrating experiment to test for synergistic effects of isochronic stellate cells on microcircuit maturation. Left: schematic of MEC layer 2 network. Every circle represents a neuron. Neurons with the same color share the same birthdate. Circles with a red border indicate neurons infected by the viral mix. In one experiment, we silenced the isochronic cohort of MEC-L2 excitatory cells born at E12. In another, we silenced a comparable fraction of neurons whose labelling was independent of neurogenesis (i.e. random cells). The E12 isochronic cohort was primed for silencing by injecting AAV1-CaMKII-Cre *in utero* as previously described. Infected cells were then targeted with the Cre-dependent virus AAV2-Syn-DIO-hM4D(Gi)-mCherry at P1 (“Isochronic Cells”). To label a comparable fraction of neurons randomly (“Random Cells”), we injected a viral mix postnatally in order to avoid any bias of birthdating (AAVs are not intrinsically tropic for cells based on birthdate, and the probability of infecting a cell more likely reflects viral titer and proximity to the site of injection). A mix containing AAV1-CaMKII-Cre and AAV2-Syn-DIO-hM4D(Gi)-mCherry was injected at P1. The two viruses were mixed in proportions that allowed labelling of a sparse population of excitatory cells in MEC-L2 (proportion in the mix was 9:1 for the Cre-carrying and the Cre-dependent viruses, respectively). CNO was delivered by subcutaneously implanted minipumps during multiple windows of microcircuit maturation (w1 to w4, corresponding to P14-P17, P17-P20, P20-P23, and P23-P26, respectively). Each mouse received CNO for a single window, selected from the set of consecutive windows that were included to make sure that the lack of an effect on development could be attributed specifically to the ontogeny of the cells silenced. **(B)** Fraction of NeuN+ neurons exhibiting nuclear expression of c-FOS (c-FOS+) across subdivisions of the transverse entorhinal-hippocampal circuit in control animals (black) and silenced animals (silencing performed in w1. Orange: silencing of isochronic cells born on E12; green: silencing of a comparable fraction of excitatory neuron in MEC-L2 independently of their molecular identity, referred to as “Random cells – entire network”; blue: silencing of a comparable fraction of stellate cells in MEC-L2, referred to as “Random cells – stellate cells”). y axis: Fraction of double positive NeuN/c-FOS neurons. 0: no neuron expresses c-FOS; 1: all neurons express c-FOS). Note that DREADD-mediated silencing induced a decrease in the fraction of cells expressing c-FOS throughout the entorhinal-hippocampal network only when isochronic cells were silenced, and not if random cells were targeted. Note also that upon silencing, MEC-L2 exhibited a decrease in c-FOS expression in every silencing group, $t > 6.92$ and $P < 0.01$. **(C)** The effect of silencing on DCX– and PV+ neurons was specific to the early window of

circuit maturation (w1) as no effect could be observed when CNO was delivered at later time points (w2 and w3). Note how, for DCX expression in stellate and pyramidal cells and for PV expression in interneurons, the curves for random, isochronic and control groups overlap for CNO delivery during either w2 or w3 (comparison between control, isochronic and random groups; 2-way ANOVA with Group and Segment as factors for all combinations among CNO delivery windows: Group: $F(1,32) < 3.40$; $P > 0.08$; Group \times Segment: $F(7, 32) < 3.82$, $P > 0.21$).

References and Notes

1. W. Penfield, W. P. E. Boldrey, Somatic motor and sensory representation in the cerebral cortex of man as studied by electrical stimulation. *Brain* **60**, 389–443 (1937). [doi:10.1093/brain/60.4.389](https://doi.org/10.1093/brain/60.4.389)
2. V. B. Mountcastle, Modality and topographic properties of single neurons of cat's somatic sensory cortex. *J. Neurophysiol.* **20**, 408–434 (1957). [Medline](#)
3. D. H. Hubel, T. N. Wiesel, Receptive fields, binocular interaction and functional architecture in the cat's visual cortex. *J. Physiol.* **160**, 106–154 (1962). [doi:10.1113/jphysiol.1962.sp006837](https://doi.org/10.1113/jphysiol.1962.sp006837) [Medline](#)
4. A. D. Huberman, M. B. Feller, B. Chapman, Mechanisms underlying development of visual maps and receptive fields. *Annu. Rev. Neurosci.* **31**, 479–509 (2008). [doi:10.1146/annurev.neuro.31.060407.125533](https://doi.org/10.1146/annurev.neuro.31.060407.125533) [Medline](#)
5. T. N. Wiesel, D. H. Hubel, Effects of visual deprivation on morphology and physiology of cells in the cat's lateral geniculate body. *J. Neurophysiol.* **26**, 978–993 (1963). [Medline](#)
6. D. H. Hubel, T. N. Wiesel, Receptive fields of cells in striate cortex of very young, visually inexperienced kittens. *J. Neurophysiol.* **26**, 994–1002 (1963). [Medline](#)
7. L. Galli, L. Maffei, Spontaneous impulse activity of rat retinal ganglion cells in prenatal life. *Science* **242**, 90–91 (1988). [doi:10.1126/science.3175637](https://doi.org/10.1126/science.3175637) [Medline](#)
8. L. C. Katz, C. J. Shatz, Synaptic activity and the construction of cortical circuits. *Science* **274**, 1133–1138 (1996). [doi:10.1126/science.274.5290.1133](https://doi.org/10.1126/science.274.5290.1133) [Medline](#)
9. D. C. Rowland, Y. Roudi, M. B. Moser, E. I. Moser, Ten years of grid cells. *Annu. Rev. Neurosci.* **39**, 19–40 (2016). [doi:10.1146/annurev-neuro-070815-013824](https://doi.org/10.1146/annurev-neuro-070815-013824) [Medline](#)
10. E. I. Moser, Y. Roudi, M. P. Witter, C. Kentros, T. Bonhoeffer, M.-B. Moser, Grid cells and cortical representation. *Nat. Rev. Neurosci.* **15**, 466–481 (2014). [doi:10.1038/nrn3766](https://doi.org/10.1038/nrn3766) [Medline](#)
11. S. R. y Cajal, Estructura del asta de Ammon y fascia dentata. *Ann. Soc. Esp. Hist. Nat.* **22**, 53–114 (1893).
12. L. de Nó, Studies on the structure of the cerebral cortex. *J. Psychol. Neurol.* **45**, 381–438 (1933).
13. M. P. Witter, E. I. Moser, Spatial representation and the architecture of the entorhinal cortex. *Trends Neurosci.* **29**, 671–678 (2006). [doi:10.1016/j.tins.2006.10.003](https://doi.org/10.1016/j.tins.2006.10.003) [Medline](#)
14. N. Cappaert, N. Van Strien, M. Witter, *Hippocampal Formation*. The rat nervous system (2015), pp. 511–573.
15. R. F. Langston, J. A. Ainge, J. J. Couey, C. B. Canto, T. L. Bjerknes, M. P. Witter, E. I. Moser, M.-B. Moser, Development of the spatial representation system in the rat. *Science* **328**, 1576–1580 (2010). [doi:10.1126/science.1188210](https://doi.org/10.1126/science.1188210) [Medline](#)
16. T. J. Wills, F. Cacucci, N. Burgess, J. O'Keefe, Development of the hippocampal cognitive map in preweanling rats. *Science* **328**, 1573–1576 (2010). [doi:10.1126/science.1188224](https://doi.org/10.1126/science.1188224) [Medline](#)

17. T. L. Bjerknes, E. I. Moser, M. B. Moser, Representation of geometric borders in the developing rat. *Neuron* **82**, 71–78 (2014). [doi:10.1016/j.neuron.2014.02.014](https://doi.org/10.1016/j.neuron.2014.02.014) [Medline](#)
18. T. L. Bjerknes, R. F. Langston, I. U. Kruge, E. I. Moser, M. B. Moser, Coherence among head direction cells before eye opening in rat pups. *Curr. Biol.* **25**, 103–108 (2015). [doi:10.1016/j.cub.2014.11.009](https://doi.org/10.1016/j.cub.2014.11.009) [Medline](#)
19. L. Muessig, J. Hauser, T. J. Wills, F. Cacucci, A developmental switch in place cell accuracy coincides with grid cell maturation. *Neuron* **86**, 1167–1173 (2015). [doi:10.1016/j.neuron.2015.05.011](https://doi.org/10.1016/j.neuron.2015.05.011) [Medline](#)
20. J. G. Gleeson, P. T. Lin, L. A. Flanagan, C. A. Walsh, Doublecortin is a microtubule-associated protein and is expressed widely by migrating neurons. *Neuron* **23**, 257–271 (1999). [doi:10.1016/S0896-6273\(00\)80778-3](https://doi.org/10.1016/S0896-6273(00)80778-3) [Medline](#)
21. J. Nacher, C. Crespo, B. S. McEwen, Doublecortin expression in the adult rat telencephalon. *Eur. J. Neurosci.* **14**, 629–644 (2001). [doi:10.1046/j.0953-816x.2001.01683.x](https://doi.org/10.1046/j.0953-816x.2001.01683.x) [Medline](#)
22. H. van Praag, G. Kempermann, F. H. Gage, Running increases cell proliferation and neurogenesis in the adult mouse dentate gyrus. *Nat. Neurosci.* **2**, 266–270 (1999). [doi:10.1038/6368](https://doi.org/10.1038/6368) [Medline](#)
23. D. Doischer, J. A. Hosp, Y. Yanagawa, K. Obata, P. Jonas, I. Vida, M. Bartos, Postnatal differentiation of basket cells from slow to fast signaling devices. *J. Neurosci.* **28**, 12956–12968 (2008). [doi:10.1523/JNEUROSCI.2890-08.2008](https://doi.org/10.1523/JNEUROSCI.2890-08.2008) [Medline](#)
24. S. Dieck, L. Sanmartí-Vila, K. Langnaese, K. Richter, S. Kindler, A. Soyke, H. Wex, K. H. Smalla, U. Kämpf, J. T. Fränzer, M. Stumm, C. C. Garner, E. D. Gundelfinger, Bassoon, a novel zinc-finger CAG/glutamine-repeat protein selectively localized at the active zone of presynaptic nerve terminals. *J. Cell Biol.* **142**, 499–509 (1998). [doi:10.1083/jcb.142.2.499](https://doi.org/10.1083/jcb.142.2.499) [Medline](#)
25. J. B. Angevine Jr., Time of neuron origin in the hippocampal region. An autoradiographic study in the mouse. *Exp. Neurol. Suppl.* **2**, 2, 1–70 (1965). [Medline](#)
26. Y. Deguchi, F. Donato, I. Galimberti, E. Cabuy, P. Caroni, Temporally matched subpopulations of selectively interconnected principal neurons in the hippocampus. *Nat. Neurosci.* **14**, 495–504 (2011). [doi:10.1038/nn.2768](https://doi.org/10.1038/nn.2768) [Medline](#)
27. C. Miao, Q. Cao, H. T. Ito, H. Yamahachi, M. P. Witter, M.-B. Moser, E. I. Moser, Hippocampal Remapping after Partial Inactivation of the Medial Entorhinal Cortex. *Neuron* **88**, 590–603 (2015). [doi:10.1016/j.neuron.2015.09.051](https://doi.org/10.1016/j.neuron.2015.09.051) [Medline](#)
28. S. Ray, M. Brecht, Structural development and dorsoventral maturation of the medial entorhinal cortex. *eLife* **5**, e13343 (2016). [doi:10.7554/eLife.13343](https://doi.org/10.7554/eLife.13343) [Medline](#)
29. L. Telley, S. Govindan, J. Prados, I. Stevant, S. Nef, E. Dermitzakis, A. Dayer, D. Jabaudon, Sequential transcriptional waves direct the differentiation of newborn neurons in the mouse neocortex. *Science* **351**, 1443–1446 (2016). [doi:10.1126/science.aad8361](https://doi.org/10.1126/science.aad8361) [Medline](#)
30. J. B. Angevine Jr., R. L. Sidman, Autoradiographic study of cell migration during histogenesis of cerebral cortex in the mouse. *Nature* **192**, 766–768 (1961). [doi:10.1038/192766b0](https://doi.org/10.1038/192766b0) [Medline](#)

31. P. Rakic, Neurons in rhesus monkey visual cortex: Systematic relation between time of origin and eventual disposition. *Science* **183**, 425–427 (1974).
[doi:10.1126/science.183.4123.425](https://doi.org/10.1126/science.183.4123.425) [Medline](#)
32. B. L. McNaughton, F. P. Battaglia, O. Jensen, E. I. Moser, M. B. Moser, Path integration and the neural basis of the ‘cognitive map’. *Nat. Rev. Neurosci.* **7**, 663–678 (2006).
[doi:10.1038/nrn1932](https://doi.org/10.1038/nrn1932) [Medline](#)
33. Y. Burak, I. R. Fiete, Accurate path integration in continuous attractor network models of grid cells. *PLOS Comput. Biol.* **5**, e1000291 (2009). [doi:10.1371/journal.pcbi.1000291](https://doi.org/10.1371/journal.pcbi.1000291) [Medline](#)
34. J. J. Couey, A. Witoelar, S.-J. Zhang, K. Zheng, J. Ye, B. Dunn, R. Czajkowski, M.-B. Moser, E. I. Moser, Y. Roudi, M. P. Witter, Recurrent inhibitory circuitry as a mechanism for grid formation. *Nat. Neurosci.* **16**, 318–324 (2013). [doi:10.1038/nn.3310](https://doi.org/10.1038/nn.3310) [Medline](#)
35. M. C. Fuhs, D. S. Touretzky, A spin glass model of path integration in rat medial entorhinal cortex. *J. Neurosci.* **26**, 4266–4276 (2006). [doi:10.1523/JNEUROSCI.4353-05.2006](https://doi.org/10.1523/JNEUROSCI.4353-05.2006) [Medline](#)
36. T. Bonnevie, B. Dunn, M. Fyhn, T. Hafting, D. Derdikman, J. L. Kubie, Y. Roudi, E. I. Moser, M.-B. Moser, Grid cells require excitatory drive from the hippocampus. *Nat. Neurosci.* **16**, 309–317 (2013). [doi:10.1038/nn.3311](https://doi.org/10.1038/nn.3311) [Medline](#)
37. P. Gao, M. P. Postiglione, T. G. Krieger, L. Hernandez, C. Wang, Z. Han, C. Streicher, E. Papusheva, R. Insolera, K. Chugh, O. Kodish, K. Huang, B. D. Simons, L. Luo, S. Hippenmeyer, S.-H. Shi, Deterministic progenitor behavior and unitary production of neurons in the neocortex. *Cell* **159**, 775–788 (2014). [doi:10.1016/j.cell.2014.10.027](https://doi.org/10.1016/j.cell.2014.10.027) [Medline](#)
38. H. Stensola, T. Stensola, T. Solstad, K. Frøland, M.-B. Moser, E. I. Moser, The entorhinal grid map is discretized. *Nature* **492**, 72–78 (2012). [doi:10.1038/nature11649](https://doi.org/10.1038/nature11649) [Medline](#)
39. S. Druckmann, L. Feng, B. Lee, C. Yook, T. Zhao, J. C. Magee, J. Kim, Structured synaptic connectivity between hippocampal regions. *Neuron* **81**, 629–640 (2014).
[doi:10.1016/j.neuron.2013.11.026](https://doi.org/10.1016/j.neuron.2013.11.026) [Medline](#)
40. M. Meister, R. O. Wong, D. A. Baylor, C. J. Shatz, Synchronous bursts of action potentials in ganglion cells of the developing mammalian retina. *Science* **252**, 939–943 (1991).
[doi:10.1126/science.2035024](https://doi.org/10.1126/science.2035024) [Medline](#)
41. C. S. Goodman, C. J. Shatz, Developmental mechanisms that generate precise patterns of neuronal connectivity. *Cell* **72** (Suppl), 77–98 (1993). [doi:10.1016/S0092-8674\(05\)80030-3](https://doi.org/10.1016/S0092-8674(05)80030-3) [Medline](#)
42. X. Leinekugel, R. Khazipov, R. Cannon, H. Hirase, Y. Ben-Ari, G. Buzsáki, Correlated bursts of activity in the neonatal hippocampus in vivo. *Science* **296**, 2049–2052 (2002).
[doi:10.1126/science.1071111](https://doi.org/10.1126/science.1071111) [Medline](#)
43. H. S. Burr, The effects of the removal of the nasal pits in *Amblystoma* embryos. *J. Exp. Zool.* **20**, 27–57 (1916). [doi:10.1002/jez.1400200202](https://doi.org/10.1002/jez.1400200202)

44. R. Levi-Montalcini, The development to the acoustico-vestibular centers in the chick embryo in the absence of the afferent root fibers and of descending fiber tracts. *J. Comp. Neurol.* **91**, 209–241, illust3 (1949). [doi:10.1002/cne.900910204](https://doi.org/10.1002/cne.900910204) [Medline](#)
45. L. Dryer, P. P. Graziadei, Influence of the olfactory organ on brain development. *Perspect. Dev. Neurobiol.* **2**, 163–174 (1994). [Medline](#)
46. P. Rakic, Specification of cerebral cortical areas. *Science* **241**, 170–176 (1988). [doi:10.1126/science.3291116](https://doi.org/10.1126/science.3291116) [Medline](#)
47. G. López-Bendito, Z. Molnár, Thalamocortical development: How are we going to get there? *Nat. Rev. Neurosci.* **4**, 276–289 (2003). [doi:10.1038/nrn1075](https://doi.org/10.1038/nrn1075) [Medline](#)
48. P. Franklin, *Paxinos and Franklin's the Mouse Brain in Stereotaxic Coordinates* (Elsevier, Academic Press, ed. 4, 2012).
49. P. Andersen, T. V. Bliss, K. K. Skrede, Lamellar organization of hippocampal excitatory pathways. *Exp. Brain Res.* **13**, 222–238 (1971). [doi:10.1007/BF00234087](https://doi.org/10.1007/BF00234087) [Medline](#)
50. O. Steward, Topographic organization of the projections from the entorhinal area to the hippocampal formation of the rat. *J. Comp. Neurol.* **167**, 285–314 (1976). [doi:10.1002/cne.901670303](https://doi.org/10.1002/cne.901670303) [Medline](#)
51. L. W. Swanson, W. M. Cowan, An autoradiographic study of the organization of the efferent connections of the hippocampal formation in the rat. *J. Comp. Neurol.* **172**, 49–84 (1977). [doi:10.1002/cne.901720104](https://doi.org/10.1002/cne.901720104) [Medline](#)
52. M. F. Yeckel, T. W. Berger, Feedforward excitation of the hippocampus by afferents from the entorhinal cortex: Redefinition of the role of the trisynaptic pathway. *Proc. Natl. Acad. Sci. U.S.A.* **87**, 5832–5836 (1990). [doi:10.1073/pnas.87.15.5832](https://doi.org/10.1073/pnas.87.15.5832) [Medline](#)
53. A. Hjorth-Simonsen, Hippocampal efferents to the ipsilateral entorhinal area: An experimental study in the rat. *J. Comp. Neurol.* **142**, 417–437 (1971). [doi:10.1002/cne.901420403](https://doi.org/10.1002/cne.901420403) [Medline](#)
54. J. M. Wojtowicz, N. Kee, BrdU assay for neurogenesis in rodents. *Nat. Protoc.* **1**, 1399–1405 (2006). [doi:10.1038/nprot.2006.224](https://doi.org/10.1038/nprot.2006.224) [Medline](#)
55. F. Donato, S. B. Rompani, P. Caroni, Parvalbumin-expressing basket-cell network plasticity induced by experience regulates adult learning. *Nature* **504**, 272–276 (2013). [doi:10.1038/nature12866](https://doi.org/10.1038/nature12866) [Medline](#)
56. C. Varga, S. Y. Lee, I. Soltesz, Target-selective GABAergic control of entorhinal cortex output. *Nat. Neurosci.* **13**, 822–824 (2010). [doi:10.1038/nn.2570](https://doi.org/10.1038/nn.2570) [Medline](#)